Inaugural - Dissertation

zur

Erlangung der Doktorwürde

der

Naturwissenschaftlich-Mathematischen

Gesamtfakultät

der

Ruprecht-Karls-Universität

Heidelberg

vorgelegt von

Dipl.-Chem. Marco Schwieder

geboren in Kulmbach

Tag der mündlichen Prüfung: 12. Februar 2009

Hierarchical Nanopatterns for Cell Adhesion Studies

Gutachter: Prof. Dr. Joachim P. Spatz

PD Dr. Reiner Dahint

Contents

Summary

Hierarchical nanopatterned interfaces are an intriguing tool to study clustering processes of proteins like for example integrins that mediate cell adhesion. The aim of this work is the development of innovative methods for the fabrication of hierarchical micro-nanopatterned surfaces and the use of such systems as platforms to study cell adhesion.

In the first part of this work different approaches are presented which are suitable for preparing micro-nanopatterned interfaces at a large scale and high sample throughput as required for biological studies. Nanopatterning is achieved by employing diblock copolymer lithography, a method previously reported to be suitable for the fabrication of extended arrays of noble metal nanoparticles by pure self-assembly. The particles are thereby embedded in a micellar shell built up by the polymer, which can be transferred to solid interfaces. Within this work the method has been combined with conventional lithographic techniques to control the particle orientation on discrete areas on the substrate material with single particle precision. Electron beam lithography was used to immobilize gold particles by cross-linking the polymeric matrix with a focused electron beam. The benefits of high precision single particle deposition and arbitrary pattern design of this technique are opposed by the lack of ability to cover areas larger than a square millimeter in one day exposure time. To overcome this drawback, nanopatterned silicon chips were completely coated with an electron sensitive resist that covered all particles on the substrate. After illuminating the resist by electron beam lithography in desired areas, the unexposed parts including the underlying particles could be removed. Washing off the protecting resist in exposed parts revealed the gold particles pattern. With this technique exposed areas could be increased to square centimeter areas within one day exposure time. As a further approach a new method was developed by exposing the substrate through a metal grid to electrons emitted by an electron flood gun rather than scanning the substrate by a focused beam. Micropatterned areas of several square centimeters could be prepared within minutes, even on non-conductive glass substrates. The three different approaches now provide a toolbox out of which a method can be chosen that suits the respective scientific purpose. Possibilities range

from single particle deposition to larger scale arbitrary patterns, that can even be transferred to non-conductive and transparent substrates.

The second part of the work, the cellular interactions of rat embryonic fibroblasts (REF) and dendritic cells (DC) with the biofunctionalized micro - nanopatterns produced were studied. Biofunctionalization included linkage of a cell receptor addressing peptide to the nano-particles and a protein repellent layer in between to avoid unspecific interaction. Fluorescent and electron microscopy images revealed, that cellular anchor points are confined to the underlying micro-nanopattern of gold particles. Intracellular actin networks connect to these protein anchor points, forming so called focal adhesions, and thereby mediate mechanical stress. At sizes of the squared adhesive patches of $\geq 1\ \mu m$ actin fibers connected to one adhesive patch. Whereas, if patterns consisted of squared patches of $\leq 500\ nm$ side length the actin fibers bridged these pattern gaps over several adhesion domains. Patterns with edge lengths of 100 nm comprising 6 ± 1 particles per patch were found to be the minimum number of adhesion receptors that need to cluster in order to induce adhesion. Cell-surface interactions have also been studied with dendritic cells, that play a key role in the immune system since they capture antigens in peripheral tissues and migrate to lymph nodes to present the processed antigen to T-cells and trigger an immune response. In contrast to fibroblasts, DCs were also able to adhere to gold particles that were functionalized with a control peptide that does not address integrins and to particles that were not functionalized at all. Additionally DC adhesion could be induced even on homogeneous patterns with spacings of up to 130 nm. Dendritic anchor points were confined to squared adhesive patches if the pattern comprised edge lengths of 5 μm or 10 μm, but were able to bridge pattern gaps if hierarchical structures consisted of 1 μm and 500 nm adhesive areas.

Zusammenfassung

Hierarchische Nanostrukturen sind ein wichtiges Werkzeug zur Untersuchung kooperativer biologischer Prozesse. Ziel dieser Arbeit war die Entwicklung neuartiger Verfahren zur Herstellung von biofunktionalisierten Mikro-/Nanostrukturierten Oberflächen und deren Anwendung als Substrat zur Untersuchung Integrin vermittelter Zelladhsion.

Der erste Teil dieser Arbeit umfasst die Entwicklung innovativer Methoden zur Herstellung Mikro-/Nanostrukturierter Partikelfelder. Die weitere Verwendung dieser Substrate zur Erforschung biologisch relevanter Fragestellungen erfordert dabei den Einsatz kostengünstiger Verfahren die eine großflächige Strukturierung mit hohem Probendurchsatz ermöglichen. Mizellare Zweiblock-Coploymer Lithographie wurde zur Darstellung metallischer Nanopartikelmasken eingesetzt. Hierbei werden mit Metallsalzen beladene Polymermizellen durch reine Selbstorganisation auf Oberflächen übertragen und bilden dabei regelmäßig angeordnete Nanopartikel. Dieses Verfahren wurde im Rahmen der Arbeit mit verschiedenen konventionellen Lithographietechniken kombiniert. Durch den Einsatz von Elektronenstrahllithographie kann die den Metallkern umgebende Polymermatrix auf der Oberfläche vernetzt werden und so selbst einzelne Partikel selektiv immobilisiert werden. Dieser hohen Präzision steht jedoch die geringe Strukturierungsgeschwindigkeit von wenigen Quadratmillimetern pro Tag gegenüber. Um diesen Nachteil zu umgehen wurden Partikel bedeckte Siliziumchips mit einem elektronenempfindlichen Lack beschichtet. Durch die Bestrahlung des Substrats mit einem fokussierten Elektronenstrahl wurde der Lack an den entsprechenden Stellen immobilisiert und konnte an den übrigen Flächen zusammen mit den Partikeln entfernt werden. Die Mikro-/Nanostruktur konnte durch Abwaschen des Lacks über den verbleibenden Partikeln freigelegt werden. Durch dieses Verfahren konnte die belichtete Fläche pro Tag auf einen Quadratzentimeter erhöht werden. Durch Bestrahlung des Substrats mit einer unfokussierten Elektronenquelle (flood-gun) durch ein Metallgitter konnten Mikro-/Nanostrukturen von einigen Quadratzentimetern innerhalb von Minuten auch auf nichtleitenden Glassubstraten erzeugt werden. Die drei verschiedenen Methoden stellen damit eine Reihe von Werkzeugen dar die nun, entsprechend der jeweiligen wissenschaftlichen

Zielsetzung eingesetzt werden können. Die Strukturierungsmöglichkeiten reichen von einzelnen Partikeln bis hin zu großflächigen aperiodischen Mustern auch auf nichtleitenden und transparenten Substraten.

Im zweiten Teil dieser Arbeit wurden die zellulären Wechselwirkungen von Rattenembryonenfibroblasten (REF) und dendritischen Zellen (DC) mit biofunktionalisierten Mikro-Nanostrukturen untersucht. Biofunktionalisierung umfasst dabei die Anbindung von spezifischen Peptiden an die Nanopartikel, sowie die Anbindung einer proteinabweisenden Schicht zwischen den Partikeln um unspezifische Interaktionen zu verhindern. Fluoreszenz- und Elektronenmikroskopiebilder zeigten, dass die zellulären Ankerpunkte auf die Fläche der darunterliegenden Mikro-/Nanostruktur von Goldpartikeln begrenzt sind. Intrazelluläre Aktinnetzwerke die mechanische Belastungen in der Zelle weiterleiten binden an diese Ankerpunkte und führen zur Bildung sogenannter Fokaler Adhäsionen. Bei Kantenlängen der quadratischen adhäsiven Flächen $\geq 1\ \mu m$ binden Aktinfasern zu einer dieser Flächen. Sind diese Flächen $\leq 500\ nm$ werden sie von Aktinfasern überbrückt die dann an mehrere dieser Flächen binden. Die Minimalanzahl an Integrinen die nötig sind um kooperativ Adhäsion auszulösen war bei einem Muster von 100 nm Kantenlänge, die je 6 ± 1 Partikel enthalten erreicht. Zell-Oberflächen Interaktionen wurden auch bei Dendritischen Zellen (DC) untersucht. DCs spielen eine Schlüsselrolle im Immunsystem, da sie Antigene im äußeren Gewebe abfangen, dann zu den Lymphknoten wandern um dort das Antigen T-Zellen zu präsentieren die wiederum eine Immunantwort induzieren. Im Gegensatz zu Fibroblasten waren DCs auch in der Lage an Goldpartikel zu binden die nicht funktionalisiert, oder mit einem Kontrollpeptid funktionalisiert waren, das keine Integrine adressiert. Darüberhinaus konnte Adhäsion auch auf Nanostrukturen mit einem Partikelabstand von bis zu 130 nm induziert werden. Dendritische Ankerpunkte waren auf quadratische adhäsive Flächen der darunterliegenden Mikro-Nanostruktur begrenzt, wenn die Strukturen Kantenlängen von 5 oder 10 μm umfassten. Bei Strukturen von 1 μm oder 500 nm Kantenlüge wurden diese Flächen von DCs überbrückt.

Part I

Hierarchichal Nanopatterns of Block Copolymers

Chapter

1

Introduction

1.1 Lithographic Approaches

Nanoscience and Nanotechnology have been *the* big emerging fields in science of the past two decades.[1] The unique properties and capabilities that have their origin just in the nanometer feature size of the materials are often in contrast to the properties of their bulk counterparts.[2–4] These findings were intriguing from the very beginning and still are a driving force for ongoing research. Possible high impact applications in semiconductor and pharma industry triggered a run in the underlying research fields to nanoscience in general and nanoparticles in particular. The techniques that are being used in order to reach nanometer resolution can be categorized in two opposing approaches: Bottom-up and top-down.

Techniques are considered to be bottom-up, if they involve building up structures atom-by-atom or molecule-by-molecule. There are two ways of accomplishing this. One way is to use tools to move each atom or molecule individually. Although this 'positional assembly' offers greater control over construction, it is currently very laborious and hence not suitable for industrial scales. In the second way called 'self assembly', the atoms or molecules arrange themselves into a structure due to their natural properties. Self assembly can be defined as "process of autonomous building up of ordered structures that involve pre-existing components (separate or distinct parts of a disordered structure), and can be controlled by proper design of the components."[5] Nature makes use of self assembly in multifarious ways since it is a powerful tool for fabricating supramolecular architectures.[6,7]

A prominent example for self assembly in nature is the tobacco mosaic virus

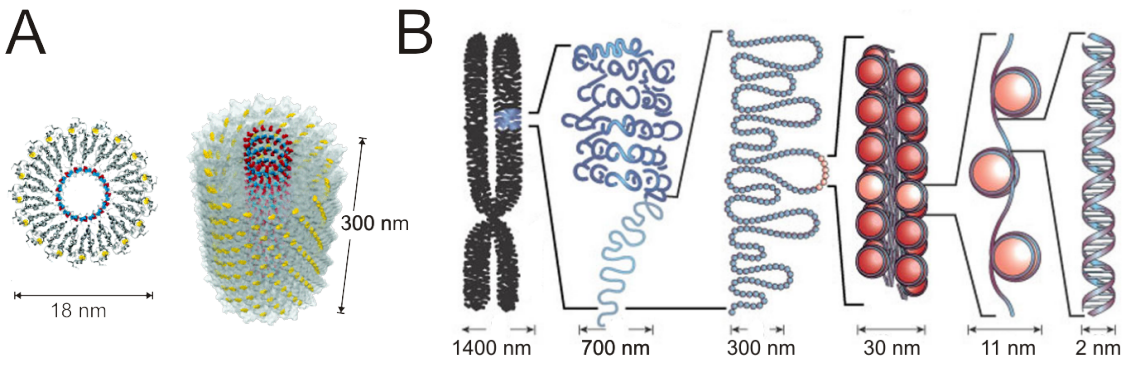

Figure 1.1: Examples for self assembly processes in nature. (A) Illustration of an tobacco mosaic virus and (B) helical organizations of DNA molecules. Adapted from [9,10]

which is a helical virus particle 300 *nm* in length and 18 *nm* in diameter. (Fig.1.1A) Its construction serves to illustrate many of the features present in self-assembling biological systems. [8,9] Even DNA molecules are constructed in a way that they can form macromolecular structures that are orders of magnitude bigger than their single subunits. [10]

Moreover, self assembly is also enormously valuable in modern material science, since it enables the preparation of structures often not accessible by other fabrication techniques. [11] Typical examples of self assembly techniques are self assembled monolayer lithography, [12] colloidal chemistry [13] and block copolymer lithography. [14–17] Self assembly techniques share the common property of being parallel, fast and hence cheap manufacturing processes, which makes them attractive for academic research *and* industrial applications.

However, to reach deeper functionality, an organization is required that goes beyond the arrangement due to inherent physical or chemical properties. An additional architecture like for example structural organization comparable to a microprocessor chip would be desirable. But complex patterns are considerably harder to achieve by pure self assembly. To bridge this gap, combinatorial approaches have come up that coined the terms 'templated' or 'guided' self assembly. Templated self assembly (TSA) is a method of eliminating defects and inducing registration and orientation in thin films of materials using artificial topographical and/or chemically patterned templates. Self assembly can hereby be confined into arbitrary geometrical designs [18] that are dictated by a pre-existing template. Prominent examples of TSA can be found for liquid crystals, [19] colloids [20] and block copolymers. [21–23] Recent efforts have also been put in aligning proteins or other biomolecules in arbitrary

patterns by microcontact printing[24] or dip-pen lithography.[25,26]

In contrast to the bottom-up approach, top-down manufacturing involves starting with bulk material and then etching, milling or machining a structure by removing material. The lithographic methods can be divided into parallel processes like photo-,[27,28] x-ray-lithography,[29,30] or serial processes like focused ion beam[31,32] and electron beam lithography.[33,34] All techniques have in common that prior to irradiation, surfaces are coated with a thin layer of light- or electron-sensitive resist. The parts that are exposed to radiation can be removed (positive resist), or are immobilized (negative resist) throughout the lift-off process, leaving the desired pattern on the substrate. Parallel processes usually involve exposure through an appropriate mask, whereas with serial processes the structure is actually "written" onto the surface by a focused beam or a stamp. Top-down technologies offer arbitrary geometrical designs and superior nanometer-level precision, however require an immense financial effort compared to most self assembly bottom-up techniques. In recent years the limits of each approach, in terms of feature size and quality that can be achieved have started to converge. Nonetheless, it is still demanding to pattern substrates over large areas with high complexity. Therefore, a combination of both approaches is the key to combine cost and efficiency advantages and to gain control over the a still critical feature size range from 0.1 - 1 μm.

The combination of top-down and bottom-up approaches has been widely used before.[18] Combining block copolymer lithography with various top down approaches allows for the generation of pattern features bridging the gap over different size scales and therefore have been termed micro-nanopatterns or hierarchical nanopatterns. Block copolymers are able to form micellar structures in solution.[35] By coating substrates with these solutions it is possible to deposit a hexagonal nano-array of metal particles with adjustable particle spacing on a surface.[36] The process consequently was termed Block Copolymer Micelle Nanolithography (BCML).[37] Block Copolymer Lithography and e-beam or photo lithography on their own are known and established techniques in the scientific community, but by combining the two approaches they form a striking tool for cell biology and single molecule surface science.

1.2 Nanobiotechnology

The trend of miniaturization and the emerging field of nanotechnology also found their way into biology.[38,39] The awareness that biology is happening on a molecular, nanoscale level has now met the possibilities to address this resolution. Accordingly there is a growing interest in nanometer scaled devices in biotechnological areas reaching from biosensors over protein nano arrays,[25] biomolecular motors[40] up to engineered nanopores[41] and DNA nanostructures for mechanics[42] and computing.[43] Like nanotechnology, biological surface science has thrived to considerable interest in the past decades. A lot of attention has not only recently been given to surface bound proteins.[44,45] However, simple adsorption techniques neither are able to provide site directed linkage, nor are they able to control the amount of bound protein. Especially protein orientation has shown to have influence on the functionality and affinity to the respective binding partner.[46,47] These drawbacks can now be overcome by coupling bioactive molecules to the nanopatterns produced by BCML and used in this work.[48]

Biologically active molecules can be linked to the surface-bound particles and thereby specifically address cellular receptors. In contrast to randomized protein adsorption to a surface, a covalent site directed linkage in case of nanopatterns that are generated by BCML is possible. Earlier efforts for studying cell-surface interactions used for example polymeric tethers to link cell-addressing peptides.[49] This method neither was able to precisely control the lateral resolution of presented ligands, nor could arrange the peptide in hierarchical patterns, which is important to get insight in structural organization of cellular adhesion components. Moreover, particle arrays produced by BCML provide the possibility of site directed linkage of the desired ligands and thereby ensure their proper orientation and biological functionality.[48] Additionally, the amount of bound protein can be easily controlled by altering the pattern spacing. Unspecific adsorption of the protein to the silicon surface in between the particles can be prevented by a layer of poly(ethylene glycol) (PEG). Moreover this pattern spacing turned out to reside in a biological relevant size range.[50] Therefore, combining BCML with bioactive linkers opened the door to a wide variety of biological active templates and possibilities taking influence on cell behavior on a molecular level.

In this work the use of hierarchical nanopatterns serves as an important, additional supplier of information. Ligands bound to gold particles are able to access single cell surface proteins. By altering the spacing of surface-bound particles, local clustering effects of these cellular proteins can be studied. However, an increased spacing is inevitably linked to a decrease in 'global' concentration of the presented ligand. Using hierarchical nanopatterns this global density can be kept constant and local clustering effects can be studied independently. Thereby a distinction of cell behavior is possible that either derive form concentration or clustering effects.

In the first part of this work newly developed approaches for micro structuring of particle nano arrays are presented in detail, explaining their advantages and drawbacks. Block copolymer micelle nanolithography will be combined with several top-down methods to yield new substrates for cell adhesion studies. Motivation was to study protein clustering effects in cellular systems *in vitro*.

The second part will consequently focus on adhesion behavior of different cell types on homogeneously and hierarchically patterned substrates of nano particles produced with techniques described in part one.

Chapter

2

Theoretical Background

2.1 Block Copolymer Micelle Nanolithography

Block copolymers can simply be considered as polymers with two or more chemically homogeneous building blocks that are joined together by covalent bonds. In the simplest case of two distinct monomers, conventionally termed A and B, a linear diblock copolymer (AB) is formed. More complex synthesis also offer the production of triblock (ABA / ABC), multiblock and starblock copolymers.[17] Usually, the respective building blocks differ considerably in their affinity towards polar or unpolar solvents, which has been subject to numerous theoretical and experimental studies over the last decades.[51–54] The so called microphase separation of diblock copolymers depends on:

1. the total degree of polymerization

$$N = (N_A + N_B) \tag{2.1}$$

2. the volume fractions of the respective blocks

$$f_A = 1 - f_B \tag{2.2}$$

3. the Flory-Higgins parameter χ

χ can be considered as a measure of incompatibility between two blocks. Therefore, the segregation product χN determines the degree of microseparation. Several

morphologies of diblock copolymer melts are obtained as a function of χN and the volume fraction of the respective block as depicted in figure 2.1.[55]

Figure 2.1: Overview of structures formed by diblock copolymers. Depending on the values of χN and the volume fraction that each block of the polymer consumes, different morphologies can be obtained. Structures of the melted diblock copolymer reach from spheres, cylinders, bicontinous, perforated layers to lamellae (from left to right). Adapted from[55]

What type of structure is being formed by the *dissolved* block copolymer is also subject to several factors. Figure 2.2 illustrates the block copolymer-like behavior of surfactants as a function of temperature, surfactant concentration and shape of the single molecule. Formation of micellar aggregates are only possible above the so called critical micellar concentration (CMC). Only for certain parameters spherical micelles are formed. Otherwise rod-like, hexagonal or even lamellar structures occur.[35]

Within this work, block copolymers consisting of polystyrene (PS) and poly-2-vinyl-pyridine (PVP) blocks have been used to produce hexagonal arrays of gold nano particles on silicon or glass surfaces. This process has been termed block copolymer micellar lithograpghy (BCML).[37] Figure 2.3 shows a structural formula of the polymer. Upon dissolving the polymer in a non-polar solvent like toluene spheric micelles are formed under the appropriate conditions. The polar PVP part aggregates in the center of the micelle whereas the non-polar PS forms a lipophilic shell. The hydrophilic PVP enriched core can be used a chemical nanoreactor. It can be loaded with various inorganic precursor compounds that yield particles out of elemental transition metals, alloys or oxides.[36,57–60] This loading can simply be accomplished by adding the precursor to the solution, which then aggregates within the micellar core. The formed micelles are hereby internally stabilized by the concentration of inorganic compounds in the core.

In experiments carried out during this work the PVP core was loaded with Tetrachloroauric(III) acid ($HAuCl_4$). This loading can be quantified according to equation 2.3. The loading parameter L is a theoretical measure of the nominal number

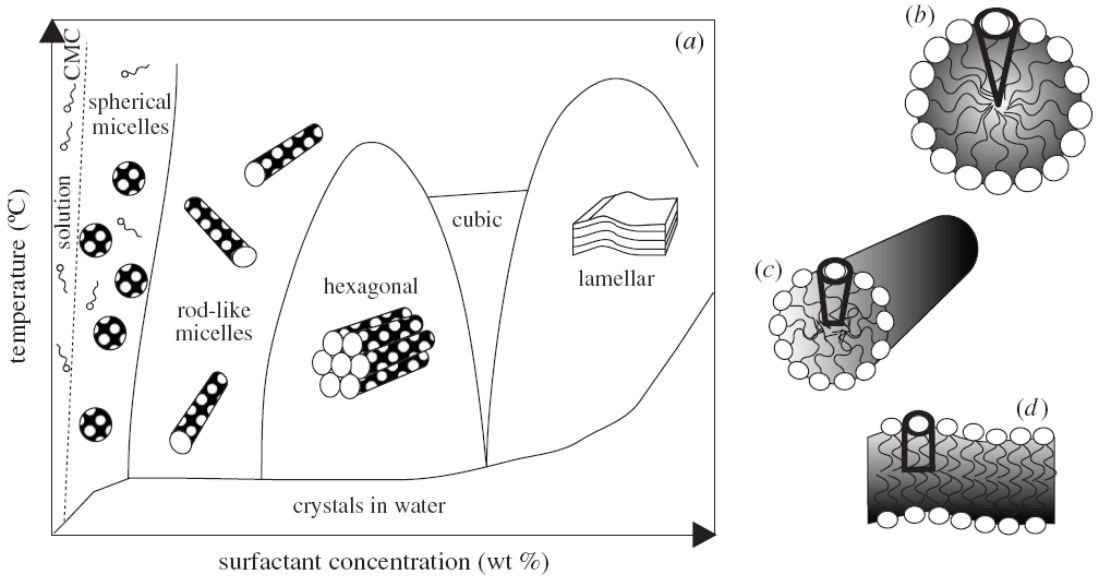

Figure 2.2: The size and shape of surfactant aggregates in solution depends strongly on the concentration and the temperature. Micelles are only formed within the window of the critical micellar concentration (CMC).(a) Further on the shape of the single molecule determines the shape of the assembled structure. Cone-shaped molecules predominantly form micellar structures(b), truncated cones from cylinders(c) and drum shaped molecules form layers.(d) [56]

of $HAuCl_4$ molecules per vinyl-pyridine (VP) unit. It is defined as the ratio of precursor-"loaded" VP units (n) against the the total number of VP units (m). The formation of micelles and the aggregation of precursor salt is illustrated in figure 2.4.

$$L = \frac{n[HAuCl_4]VP}{mVP} \tag{2.3}$$

In order to obtain hexagonal patterns of gold nano particles, the block copolymer solution has to be transferred to a surface. Since spin coating usually gives less control over the lateral order [63] dip coating was used to reach a constant lateral spacing of particles. In a proximate step the precursor salt needs to be reduced to elemental gold and the structure-bearing micellar shell around the particle needs to be removed. This is accomplished by a hydrogen plasma etching process depicted in figure 2.5. Due to Ostwald ripening smaller fractions of gold merge together to nanoparticles during the plasma process. [64]

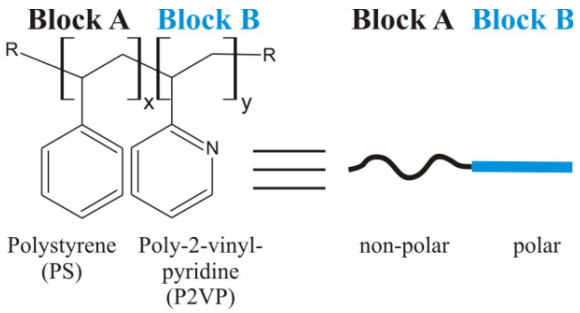

Figure 2.3: Structural formula of polystyrene-*b*-poly(2-vinyl-pyridine) block copolymer. Polystyrene (block A) represents the non-polar part (black coil), whereas poly-2-vinyl-pyridine (block B) represents the polar part. [61]

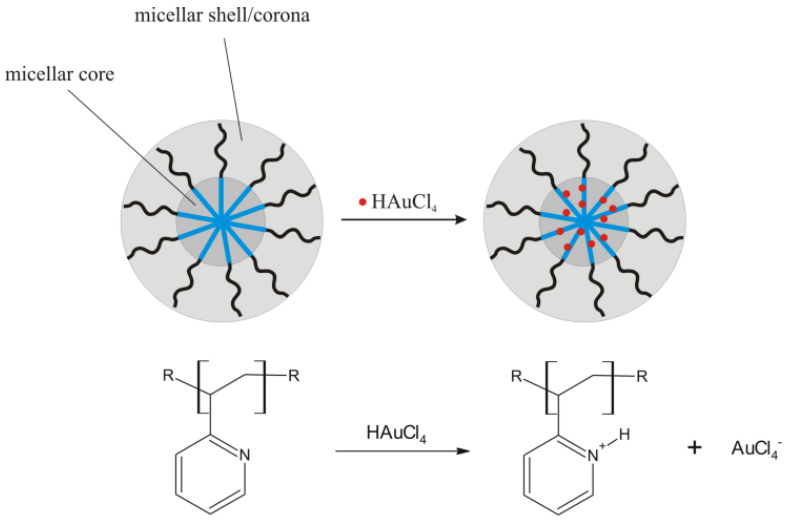

Figure 2.4: Illustration of the loading process for PS-PVP block copolymers. Upon adding $HAuCl_4$ to the solution the metallic precursor aggregates in the polar center of the micelle and additionally stabilizes the micellar structure. [61]

The spacing and the size of this hexagonal pattern of gold particles can be tuned in several ways. In first instance the molecular weight of the block copolymer determines the spacing of the pattern as depicted in figure 2.6. But also, concentration of the polymer solution as well as dipping speed influence the spacing. Especially variation of the dipping speed offers a convenient way to produce gradient spaced patterns. [65] Via electroless deposition it is even possible to subsequently increase the particle size and combine these two techniques to a two-dimensional gradient. [66]

The number of particles within a specified area can be calculated as follows. Assuming a perfect hexagonal ordered pattern the number of particles is given by

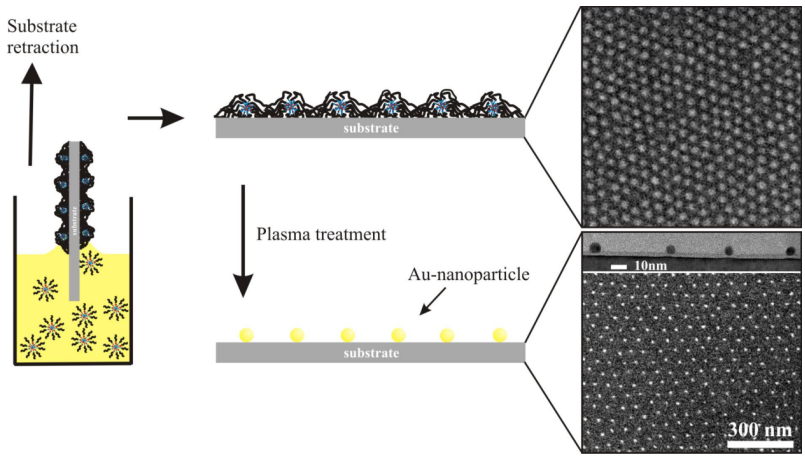

Figure 2.5: Schematic of the coating process. Glass cover slips or silicon wafers are immersed into the micellar solution and retracted at constant speed. Upon evaporation of the volatile solvent a highly ordered quasi hexagonally packed pattern is formed. After a plasma etching process the gold particle structure is revealed. Pictures on the right show the hexagonal pattern at different states of the coating process monitored by scanning electron microscopy.[61]

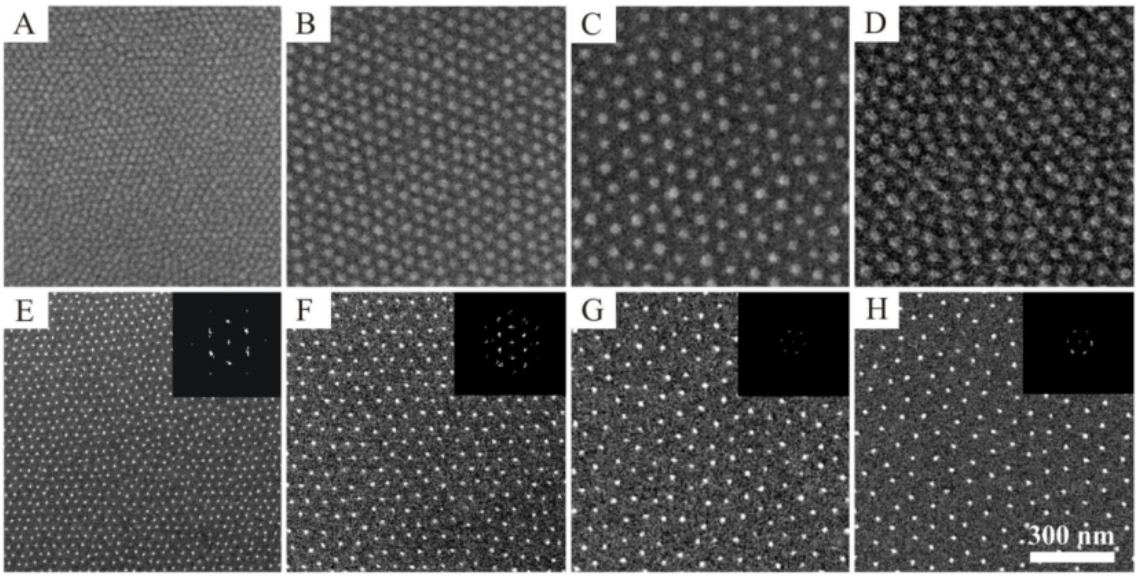

Figure 2.6: Examples of hexagonal nanopatterns on silicon wafers imaged with scanning electron microscopy (SEM). The spacing of the patterns depend on the molecular weight of the block copolymers. (A) PS(190)-*b*-P2VP(190), (B) PS(500)-*b*-P2VP(270), (C) PS(990)-*b*-P2VP(385), and (D) PS(1350)-*b*-P2VP(400). Numbers in parenthesis indicate the number of units per block. (E-H) SEM micrographs of Au nanocluster arrays after hydrogen plasma treatments of the corresponding monomicellar films from (A-D) including fourier transformed images.[62]

the relation of the area of interest to the area of the elementary cell of the pattern divided by two. The elementary cell in case of a hexagonal pattern is an equilateral triangle. Given that the area of interest is a square, the number of particles can be calculated according to equation 2.4.

$$P = \frac{2A^2}{\sqrt{3}a^2} \tag{2.4}$$

With P being the number of particles, A edge length of the squared area of interest and a edge length of equilateral triangle of the elementary cell, which during this work will equal the mean lateral spacing of particles.

2.2 Scanning Electron Microscopy

2.2.1 Electron Sources

Recognition of nanoparticles requires appropriate equipment. The method of choice is scanning electron microscopy (SEM) since it offers an easy and convenient way to image features below the resolution of the visible wavelengths.

Like optical microscopes, electron microscopes need a source of illumination. These sources usually divide up in thermionic and field emission sources to generate highly accelerated electrons. Thermionic sources like Tungsten filaments or LaB_6 crystals generate electrons simply by heating up whereas field emission relies on the fact that the strength of an electric field is considerably increased at sharp points. The electric field E depends from the applied voltage V and the radius of a (spherical) tip according to equation 2.5.

$$E = \frac{V}{r} \tag{2.5}$$

Field emission guns historically turned out to be the better choice for scanning electron microscopy because they provide a higher brightness and current density, lower energy spread and longer lifetime compared to thermionic sources.[67] Figure 2.7 shows an SEM image of a so called schottky emitter (ZrO/W-cathode). The Schottky field emission tip consists of a finely etched $< 100 >$ oriented tungsten crystal tip, with a sintered reservoir of zirconium oxide in the shank. If an electric field is generated by the extractor, the ZrO will diffuse to the cathode and form a fine tip. An opposing field is generated using the suppressor electrode to avoid

the emission of thermal electrons that are not emitted by the cathode tip but by the heated tungsten wire of the filament, which would only contribute to energy dispersion of the electron beam.[68]

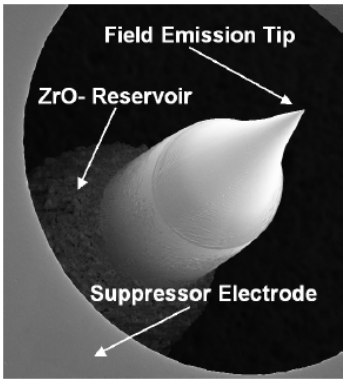

Figure 2.7: Image of a so called schottky emitter which is a field emission electron source in the electron microscope setup used in this work.[68]

Extracted electrons are accelerated by an electric field of up to 30 kV. The flood of accelerated electrons is then focused by magnetic and electrostatic lenses to a beam that scans areas of interest line by line. Electron-surface interaction at the scanned regions produce additional electrons or radiation that can be detected. See figure 2.9 for an overview. The received signal is then assembled to form a picture like one would actually "see" the specimen in high magnification. Depending on the type of radiation different detectors are used that reveal information about topographical features or material composition of the specimen.

2.2.2 Electron Interactions

When a beam of accelerated electrons hits the surface several scattering and diffraction events occur. However, electrons can be regarded as particles *or* waves according to the wave particle duality, the interactions relevant for SEM imaging are best described when looking at the electron as a dense particle. These interactions can be elastic or inelastic scattering events. Assuming the electron to be a negatively charged particle it can interact with either a dense positively charged nucleus or a more distributed electron "cloud" around the nucleus.

Elastic Scattering

In the case of elastic scattering an electron hits a specimen atom and is diverted to another direction without any loss of kinetic energy. The probability of elastic scattering increases roughly with the square of the atomic number (Z). According to equation 2.6 the probability of an elastic scattering event with an angle larger than ϕ_0 can also be described as an area of cross section Q.

$$Q(>\phi_0)[cm^2] = 1.62 \times 10^{-20}(Z^2/E^2)\cot^2(\phi_0/2) \tag{2.6}$$

Depending on Q, the average distance an electron travels in the sample between scattering events can be calculated as the so called "mean free path" λ.

$$\lambda[cm] = A/N_{0\rho}Q \tag{2.7}$$

Here, N_0 is Avogadro's number, Z is the atomic number, ρ is the density (g/cm^3) and A is the atomic weight (g/mol).

Inelastic Scattering

Inelastic scattering on the other hand describes the trajectory of an electron in the sample by a gradual loss of energy, whilst passing on the energy to generate i.e. secondary electrons or x-rays, which are then used to reveal information about the sample. Equation 2.8 calculates this loss of energy (dE) as a function of distance (ds) traveled in the specimen.[69]

$$\frac{dE}{ds}\left[\frac{keV}{cm}\right] = -2\pi e^4 N_0 \frac{Z\rho}{AE_i}\ln\left(\frac{1.166E_i}{J}\right) \tag{2.8}$$

$$J[keV] = (9.76Z + 58.5Z^{-0.19}) \times 10^{-3} \tag{2.9}$$

Here, e is the electron charge, E_i is the electron energy (keV) at any point in the specimen and J is the average loss in energy per event.[70] The described events can be simulated as shown in figure 2.8 for different accelerating voltages on a silicon sample.

Figure 2.8 illustrates how the interaction volume of electrons with the specimen depends on the accelerating voltage. A highly energetic electron beam, which has only a diameter of 1 nm can produce scattering effects up to several μm away from

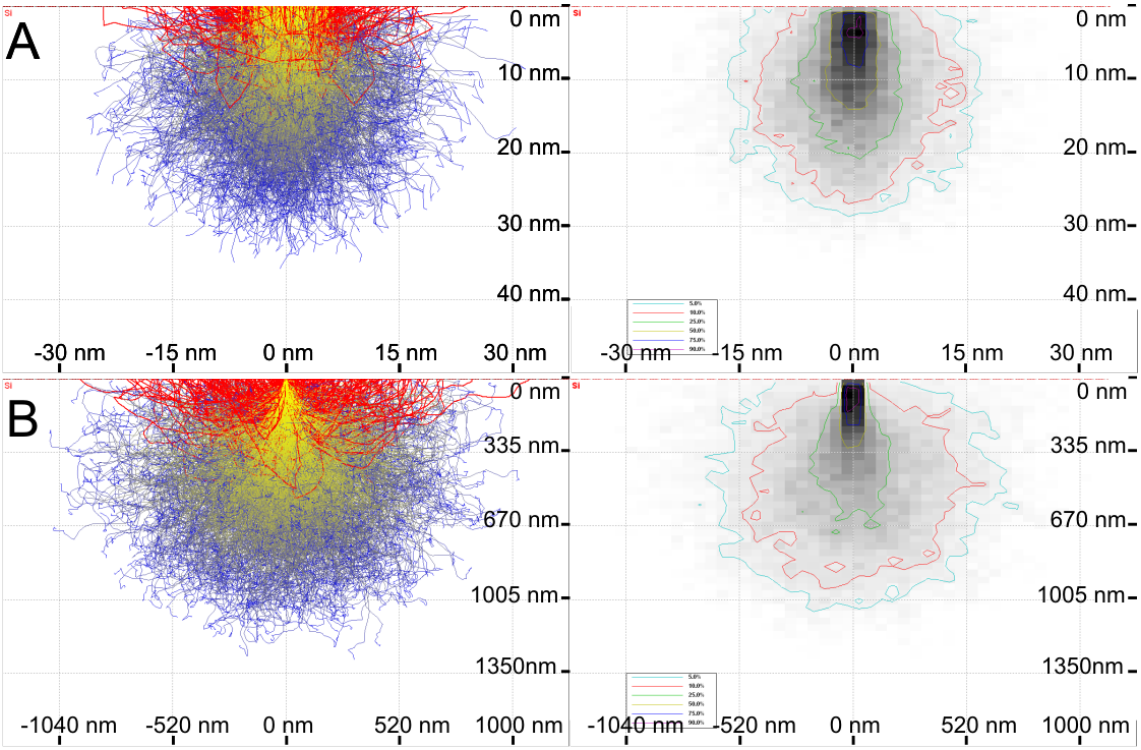

Figure 2.8: Monte Carlo simulations for a 1 kV (A) and a 10 kV (B) beam striking silicon. Left images shows the trajectories of electrons with decreasing energy from yellow to blue. Red trajectories show backscattered electrons leaving the specimen. Right images show the interaction volume with electron energies in percentage of the incident beam. Note the different scalings of A and B. Simulations were carried out with CASINO Version 2.42, Université de Sheerbrooke, Quebec, Canada.

the actual spot.

As seen in figure 2.9 a lot of information can be drawn from scattering and diffraction events of the electron beam with the specimen. However for imaging purposes usually only back scattered electrons (BSE) and secondary electrons (SE) are taken into account.

Backscattered Electrons

Backscattered electrons are defined as electrons emitted from the specimen with energies between 50 eV and the incident beam energy. These electrons undergo large-angle elastic scattering ($90° - 180°$) and leave the sample again after few or

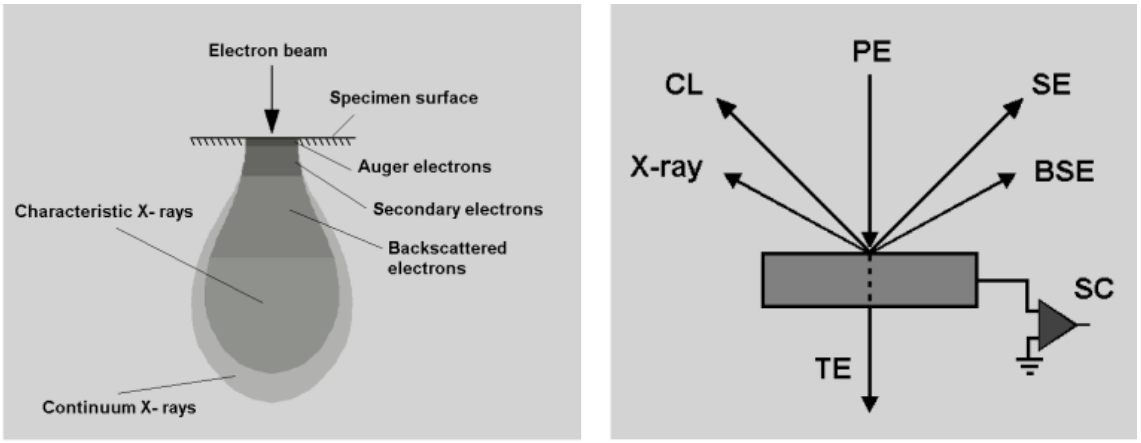

Figure 2.9: Schematic of interactions taking place when accelerated electrons hit the specimen surface. Left: The interaction volume with depicted regions out of which information bearing radiation or particles are emitted. Right: A focused beam of primary electrons (PE) penetrates the sample and generated several follow up radiations out of with detailed information can be gathered of the specimens molecular composition or topography. This includes secondary electrons (SE), backscattered electrons (BSE), X-rays, cathodoluminescense (CL) and transmitted electrons (TE). Even specimen currents (SC) can be measured. Adapted from [68]

even only one scattering event. The ratio of backscattered electrons to incident electrons is quantified according to equation 2.10. [71]

$$\eta = \frac{n_{BSE}}{n_B} = \frac{i_{BSE}}{i_B} \tag{2.10}$$

With n_B being the number of primary electrons hitting the sample and n_{BSE} the number of backscattered electrons. The yield of BSE can also be calculated according the respective beam currents of the incident beam (i_B) and backscattered electrons (i_{BSE}). The ratio η increases with higher atomic number (Z) of the specimen. Typical examples are $\eta = 0.05$ for carbon or $\eta = 0.49$ for gold, which have been calculated according to equation 2.11. [70]

$$\eta = -0.0254 + 0.016Z - 1.86 \times 10^{-4}Z^2 + 8.3 \times 10^{-7}Z^3 \tag{2.11}$$

The fact that η depends on the atomic number Z results in enhanced material contrast when detecting BSE.

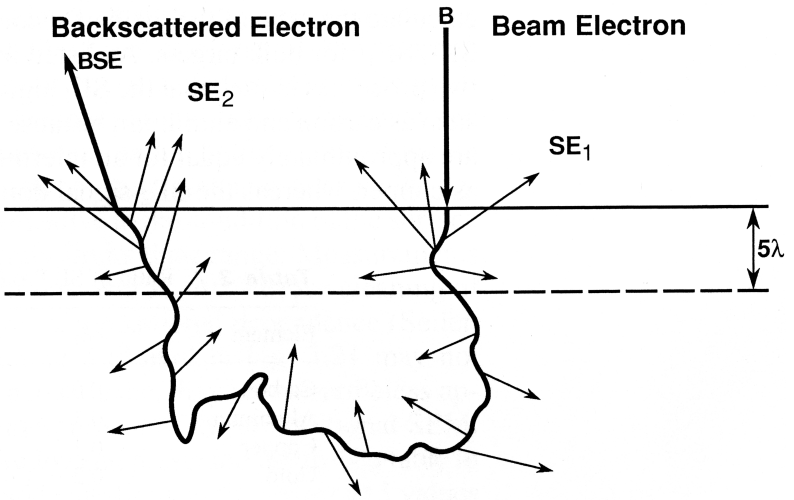

Figure 2.10: Illustration of an electron hitting the specimen and causing several inelastic scattering events. The incident energy is distributed to the generated SE. After reaching the specimen surface again the incident electron leaves the sample as BSE with decreased energy. Depending on the depth in which SE are generated they also leave the specimen and can be detected. The maximum depth up to which SE can leave the specimen has been determined to be 5λ.[70] (See equation 2.7)

Secondary Electrons

Backscattered electrons not only are elastically scattered and leave the specimen but also generate, among other effects, secondary electrons caused by subsequent inelastic scattering events. Such SE are created by ejecting electrons out of the electronic shell of the specimen atoms. Depending on how "tightly" these shell electrons are bound their energy varies. Although some SE can be of considerable high energy the vast majority of SE contributing to the signal are so called "slow" SE. Therefore, secondary electrons are considered electrons with energies lower than 50 eV. In contrast to BSE, the yield of SE is fairly independent from the atomic number of the specimen. Therefore, detectors capturing SE will not display much information on material contrast. Consequently SE2 detectors are mainly used to image topographical features. Figure 2.10 is illustrating how BSE cause SE by several scattering events passing on energy and finally leave the specimen again.

Further on, a distinction is made between secondary electrons ejected by the primary beam (SE1) and secondary electrons generated by backscattered electrons (SE2). Obviously the information carried by SE1 will generate images at a much higher spatial and compositional resolution than the one of SE2. SE2 originate

from a broader area around the focused spot of the incident beam and therefore blur the received information. Unfortunately these two kinds of secondary electrons are technically hard to distinguish since they are about equal energy.

Proximity Effect

For lithographic purposes usually an electron-sensitive resist is coated on top of a desired surface. The resist is struck by a focused electron beam and undergoes chemical changes due to the applied dose. As described above and also illustrated in several figures the incident electrons are subject to a number of scattering events. The backscattered electrons leave the sample surface again in a considerable distance from the incident beam and obviously contribute there additionally to the lithographic process when protruding the resist layer. This so called proximity effect leads to significant blurring of the desired pattern.[72]

Chapter

3

Materials and Methods

Block Copolymers have been purchased from Polymer Source Inc., Montreal, Canada and were dissolved in toluene (Merck KGaA, Darmstadt, Germany) and stirred for 24 h. Respective polymers that were used throughout this work are listed in table 3.1. $HAuCl_4$ (Sigma-Aldrich) was added to the solution according to equation 2.3 on page 15 to give a loading parameter L of 0.5 or 0.2 respectively, in case of P3499-S4VP. After dissolving the metal precursor salt, solutions were stored in darkness at room temperature.

Product ID	M_N (PS)(g/mol)	M_N (PVP)(g/mol)	M_W/ M_N
P3670-S2VP	25500	23500	1.05
P4707-S2VP	52200	34000	1.05
P4988-S2VP	110000	52000	1.15
P4554-S2VP	190000	55000	1.10
P4713-S2VP	216000	60000	1.05
P3499-S4VP	557000	75000	1.07

Table 3.1: Diblock copolymers used throughout this work

Substrate Patterning Glassware and substrates were cleaned in freshly prepared piranha solution (1:3 / H_2O_2 (30%) : *conc.* H_2SO_4) for 40 minutes, briefly rinsed in ultrapure water ($R \geq 18M\Omega$) and blow dried under a stream of nitrogen prior to contact with the polymer solution. Substrates included glass cover slips (Carl Roth & Co GmbH) and silicon wafers (Crystec, Berlin, Germany).

Samples were dip-coated with a custom made dip device. Retraction speed was

kept constant during the process. Depending on the desired spacing the speed was varied between 10-20 mm/min.

The order parameter of hexagonal arranged gold particles was calculated using an image analyzer plugin for ImageJ kindly provided by Jennifer Curtis and Phillipe Girard described earlier.[61] The tool calculates the average distance to the 6 nearest neighbors of each particle based on SEM imaging data and yields the average spacing of the particles and an order parameter $0 < \Phi < 1$. With 1 representing a perfect hexagonal pattern and 0 complete disorder. Only samples reaching an order parameter ≥ 0.5 were considered to be of sufficient pattern quality to be taken for further experiments.

Scanning Electron Microscopy A Zeiss Ultra 55 and a LEO 1530 field emission gun scanning electron microscope (Zeiss, Oberkochen, Germany) were used to monitor results. Samples were coated with a layer of ~ 5 nm carbon with a BAL-TEC MED20 sputter coater (BAL-TEC AG, Liechtenstein / Leica Microsystems, Wetzlar, Germany) to reach conductivity.

Electron Lithography Electron beam lithography was carried out with a Raith Elphy Plus system (Raith, Dortmund, Germany) attached to a Zeiss Ultra 55 SEM.

Resist Lithography: Nanopatterned 2 cm $\times$ 2 cm silicon chips cut from wafers were spincoated with electronbeam resist (AR-N7500.08, Allresist GmbH, Strausberg, Germany) to yield a layer thickness of 100 nm. The applied dose was 50 $\mu C/cm^2$ at a beam voltage of 15 kV. Samples were developed for 90 sec with AR300-47 diluted 4:1 with distilled water, rinsed in ultra pure water and dried under a stream of nitrogen. Substrate bound gold clusters were dissolved by immersing the samples for 10 min in 1%(m/V) aqueous solution of 2-aminoethanethiol and applying $3min$ of ultrasonic treatment. Protecting resist was washed off with ethanol or acetone.

Micelle electron beam lithography: Glass substrates were coated with a 5 nm layer of carbon prior to dip-coating. Non-plasma treated samples were exposed to electron beam doses of 7.5 mC/cm^2 at 1 kV unless noted differently. Lines of single particles and single particles alone were achieved by applying a dose of 50 $\mu C/cm$ or 0.1 pC respectively. Lift-off was carried out by applying an ultrasonic treatment for 5 min whilst immersing the sample in acetone.

Electron flood gun lithography: A custom made flood gun device (Floodgun FG20, SPECS GmbH, Berlin)* was used to expose samples to a flux of electrons. Electron exposures were carried out under high vacuum and with base pressures of $1 \times 10^{-7} mbar$ and doses of either 10 mC, 30 mC or 50 mC at 1 kV.

The sample was placed at $\sim$ 12 cm from the electron source and a Nickel grid with mesh sizes of 5 μm purchased from Plano GmbH (Wetzlar, Germany) served as shadow mask. For lift-off an ultrasonic bath (Bandelin Sonorex Super 10P, Berlin, Germany) was used.

*Prof. Grunze, University of Heidelberg, Applied Physical Chemistry, Im Neuenheimer Feld 253, D-69120 Heidelberg

Chapter

4

Results and Discussion

Three different approaches for hierarchical patterning of block copolymers will be shown in this part of the work. Micellar electron beam lithography described in the upcoming section has already been described before[58] but will be presented here as technique with improved precision and enhanced flexibility. Additionally, two completely new approaches have been developed that extend the possibilities of patterning to large areas and non-conductive substrates.

4.1 Micelle Electron Beam Lithography

Micelle electron beam lithography (MEBL) has already been used earlier to generate micro-patterns of nanometer sized gold particles.[58,73,74] The technique takes advantage of the fact that polymers cross-link when exposed to an electron beam.[75] As a result of the exposure the metal precursor loaded micelles are pinned to the surface. A subsequent plasma treatment of the surfaces reveals the micro-nanopattern. Figure 4.1 shows briefly the steps needed to carry out MEBL.

Major advantages of this technique are the generation of arbitrary pattern geometries and an extremely high accuracy of the lithographic process. Inherent to electron beam lithography, and in contrast to photo lithography, is the broad flexibility in pattern geometries. Photo lithography requires expensive shadow masks, through which substrates are exposed to UV-light. Once produced they have a fix pattern design and cannot be altered anymore. Whereas for e-beam exposures the pattern can be individually designed for any purpose. Especially if pattern designs

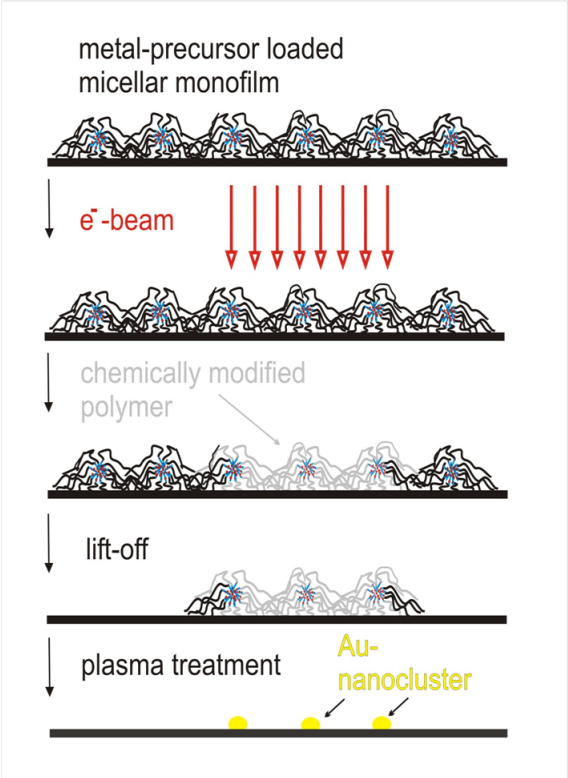

Figure 4.1: Micellar electron beam lithography (MEBL) uses a metal precursor salt loaded monolayer as negative resist on conductive substrates. The electron beam chemically modifies the polymeric structure and pins the micelles to the surface. Non-irradiated parts can be easily removed by ultrasonic treatment in acetone. After a subsequent plasma treatment the micro-nanostructure of metal particles is revealed at areas, which have been exposed to the electronic flux. [62]

need to be adjusted to experimental setups or to tackle short term questions this can be of great advantage. Moreover, the substrates are very easy to handle since the process requires only few additional steps compared to standard block copolymer lithography described in section 2.1.

On the other hand MEBL requires very high electron doses during the exposure step leading to long exposure times and hence a very limited area that can be irradiated. With the used setup and parameters exposure times of 14 hours hardly reached a size of 0.5 mm^2 exposed area. A minor drawback of MEBL is that it it only works on conductive samples. Therefore, glass substrates need to be coated with a thin layer of carbon to achieve conductivity.

In previous works MEBL already has been used to generate diverse micro-nano patterns for the proof of principle and further on for several cell adhesion studies.

A new aspect of the technique which has been revealed during this work is the flexibility and the precision of the process. With MEBL several structures have been designed and transferred to a micro-nano structure of gold particles. In order to exemplify the flexibility of this technique very complex structures like the Minerva (logo of the Max Planck Society) have been exposed, which require only minimal additional effort compared to regular patterns like arrays of squares or circles. Figure 4.2 shows the exposed structure after lift-off but before plasma treatment since at that state of the process the structure is much easier to recognize. Next to the exposed parts leftovers of disrupted polymer can be seen, which is then removed by the subsequent plasma treatment.

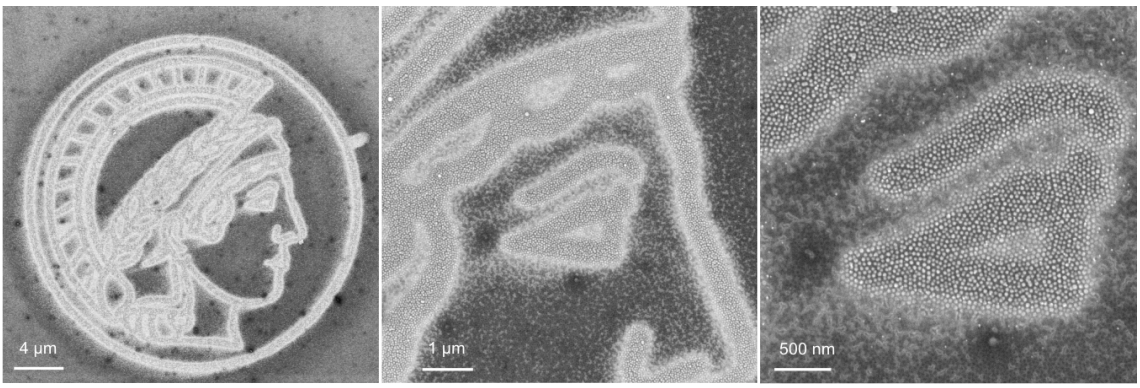

Figure 4.2: SEM image of gold nanoparticles arranged as the Minerva logo of the Max Planck Society. The shown pattern was designed and exposed during this work to exemplify the versatility of the lithographic process. The brighter appearing areas have been exposed to the electron beam and cross-linked polymer in these regions conserves particles throughout the lift-off process. Images were obtained before plasma etching to insure sufficient contrast of the sample.

Earlier efforts partly made use of this flexibility of MEBL but did not reach the accuracy that has been achieved within this work using the same technique.[58] Figure 4.3 shows single gold particles on silicon surfaces which have been immobilized by MEBL. The accuracy is sufficient to pin single block copolymer micelles in arbitrary spacings and arrangements. Left image of figure 4.3 depicts single particles that have been arranged in a quadratic pattern spaced by 500 nm. Though being very precise the electron beam is not able to capture only one particle per spot at every time. The probability that each irradiated spot actually bears only one particle is $\sim$ 80%. All other cases include no particle per spot or 2-3. Depending on the applied

dose these cases can vary in their probability to occur.

The reasons for these limits in accuracy can be found for one instance in proximity effects. As seen in figure 2.8 on page 21 the area of impact of electrons that are relevant for the lithographic process can be estimated to 30-40 *nm* in diameter. Therefore, a physical limit has been reached, which cannot be overcome. Secondly, the accuracy of MEBL strongly depends on the quality of the underlying self assembled pattern. Areas of structural defects often show clustering of metal particles. This clearly diminishes the accuracy and and leads to a less specific capturing of single particles.

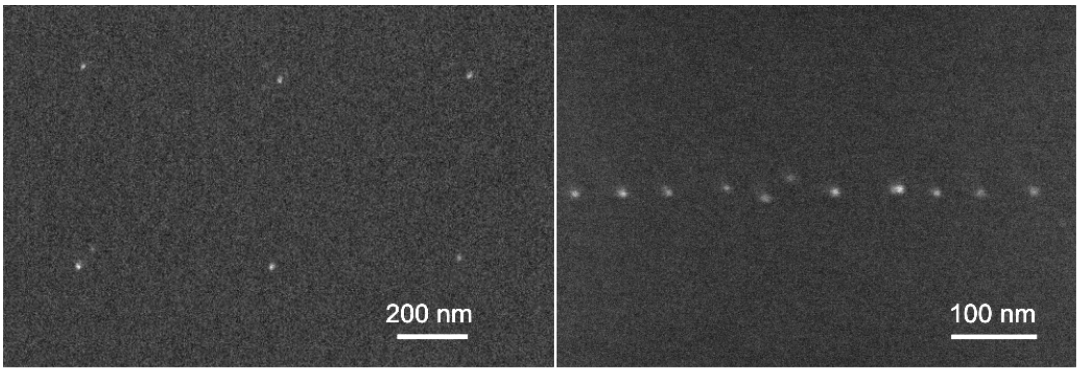

Figure 4.3: SEM images of single gold particles immobilized on a silicon surface by an electron beam

The afore mentioned influences on accuracy of course also apply for generation of lines of gold particles. But as depicted in figure 4.3 the accuracy is sufficient to produce lines of single gold particles in arbitrary geometries. In contrast to earlier strategies to generate single particle lines, the currently used procedure requires much less effort to produce the same result.[73] The techniques in the mentioned reference required additional coating of a photo or electron sensitive resist, exposure and development steps prior to dip coating. At the edges of the resist micro structure, lines of single micelles were formed in a guided self assembly-like manner. All these additional steps do not have to be carried out when using MEBL but give the same result plus the advantages that pattern geometry is not linked to a fix mask and single particle lines can be extended to defined multi-dot stripes, if this is required.

In summary it could be shown, that MEBL is a versatile tool to produce micro-nano patterns of gold particles. The striking advantage of high accuracy could be improved up to a physical limit by producing patterns with single particles and lines of single particles in any desired arrangement. Since the maximum spacing of particles produced by standard MBCL is limited to $\sim 300\ nm$ spacing this could give way to applications where optical microscopy can be used to distinguish single nano particles. Even single fluorescent molecules attached to gold nano-clusters might be made visible.

Up to now, cell adhesion studies on micro-nano patterns of gold particles have been restricted to tiny areas. But often a deeper biological insight like e.g. RNA analyses would be of interest rather than just morphology or motility of single cells. In order to gain a reliable signal of RNA analysis at least 1×10^6 cells would be needed. This would consume areas of at least $1\ cm^2$ or more, which is clearly not achievable with MEBL within a reasonable amount of time. This need inspired the development a technique that is capable of patterning large areas with a sufficient accuracy for cell adhesion studies.

4.2 Resist Electron Beam Lithography

The technique rests upon readily patterned substrates produced by standard BCML. Silicon wafers patterned with an hexagonal array of gold particles were spin coated with an electron sensitive resist that completely covered the gold particles. Upon electron beam exposure the negative resist was immobilized at irradiated areas, whereas non-irradiated parts could be easily removed by the the appropriate development solution. This revealed the nano structure only in unexposed parts whereas exposed areas still were covered and protected by a layer of resist. The unprotected gold particles could now be dissolved by immersing the substrate in an aqueous solution of 2-aminoethanethiol (Cysteamine) for 10 minutes. In order to achieve a complete particle lift-off an additional ultra sonic treatment in the same solution turned out to be necessary. After washing off the protecting resist with ethanol or acetone the micro-nano pattern was revealed. The procedure is illustrated in figure 4.4.

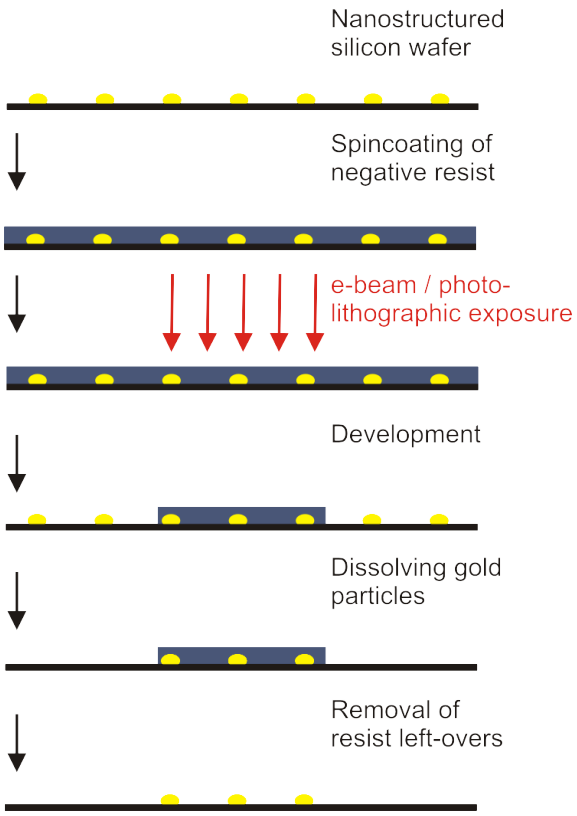

Figure 4.4: Schematic of the micro-nano patterning procedure using a spin coated resist.

To exemplify the technique, several patterns were generated and exposed. This mainly included quadratic structures of different sizes, which also will be used as cell substrates in part II. Figure 4.5 shows experimental examples of the above described process. Different states of the process are depicted. Development of unexposed resist worked completely without leaving any unwanted residues on the surface, unless blocks of 400 nm and 800 nm edge length with sharp borders. (Image A and D) Next to these blocks the underlying nanopattern can be recognized as small white spots. Subsequently uncovered nanoparticles were dissolved as described above. (Image B and E) The accuracy of the exposure process can be carried through the process steps until the actual micro-nano structure of gold dots is revealed. (Image C and F) In order to remove the covering resist blocks simple washing in Ethanol and a 10 min subsequent plasma cleaning step was sufficient.

The versatility and accuracy of the technique is illustrated in figure 4.6. Several arrangements of quadratic resist blocks are shown on top of a particle nanostructure. Figure 4.6 A and B give an overview of a typical test sample in different magnifica-

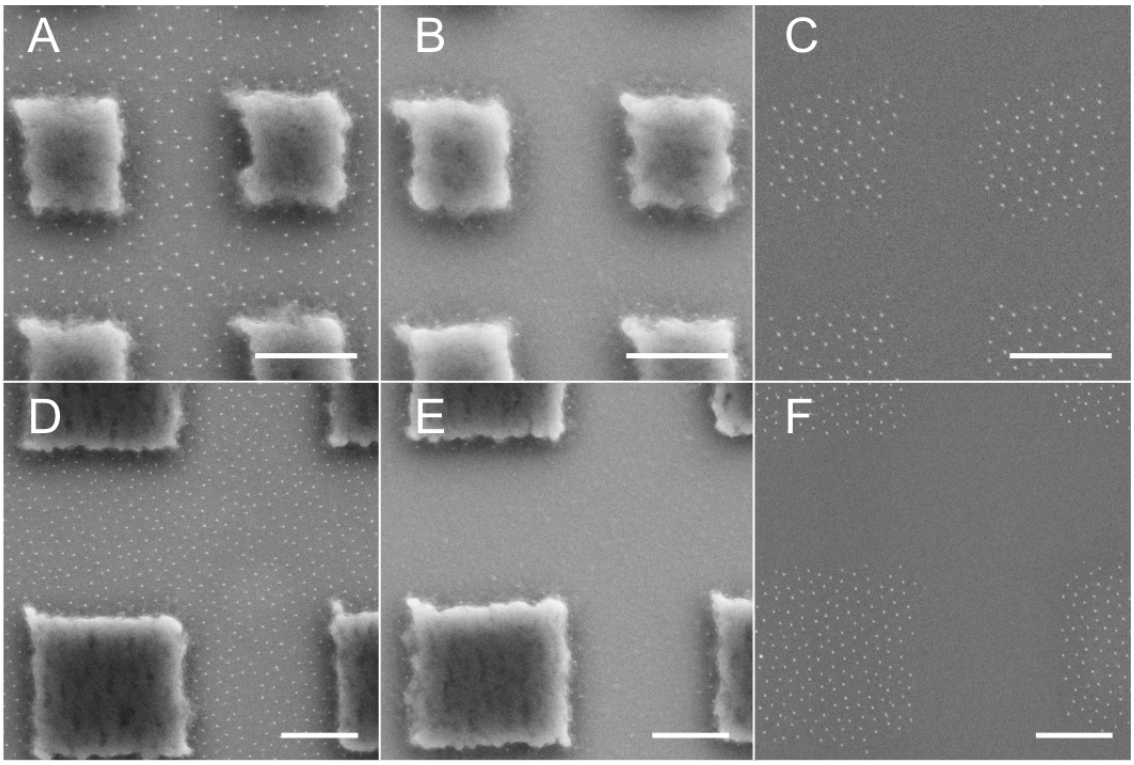

Figure 4.5: SEM images of different states in the micro patterning process via resist described in fig. 4.4. (A, D) Development of the unexposed resist. (B, E) Removal of gold particles. (C, F) Removal of exposed resist. Scale bar is 400 nm.

tions. The possibility to generate arbitrary designs is comparable to MEBL since it rests upon the same lithographic technique. Complex structures comparable to figure 4.2 proved to be feasible. (data not shown) However, considering the precision of the process it cannot compete with MEBL. Figure 4.6C shows blocks of resist after development of $\sim 80\ nm$ in diameter, which turned out to be the limit up to which a clear resist development was still possible. Next to the small blocks the underlying nanopattern is visible. But the limit of 80 nm holds true only for the development of the resist. Small blocks like depicted in image c are removed partly by the ultra sonic treatment included in the particle lift-off step. The size limit for micro-nano structures that was possible to maintain throughout the whole process turned out to be $\sim 200\ nm$ in diameter.

Compared to the technique presented in the previous section, the major advantage of the resist coating technique and the reason why the step was taken to develop a new technique is the capability of patterning large areas. The reason for this lies in the fact that the used resist only needs a fraction of the applied dose compared

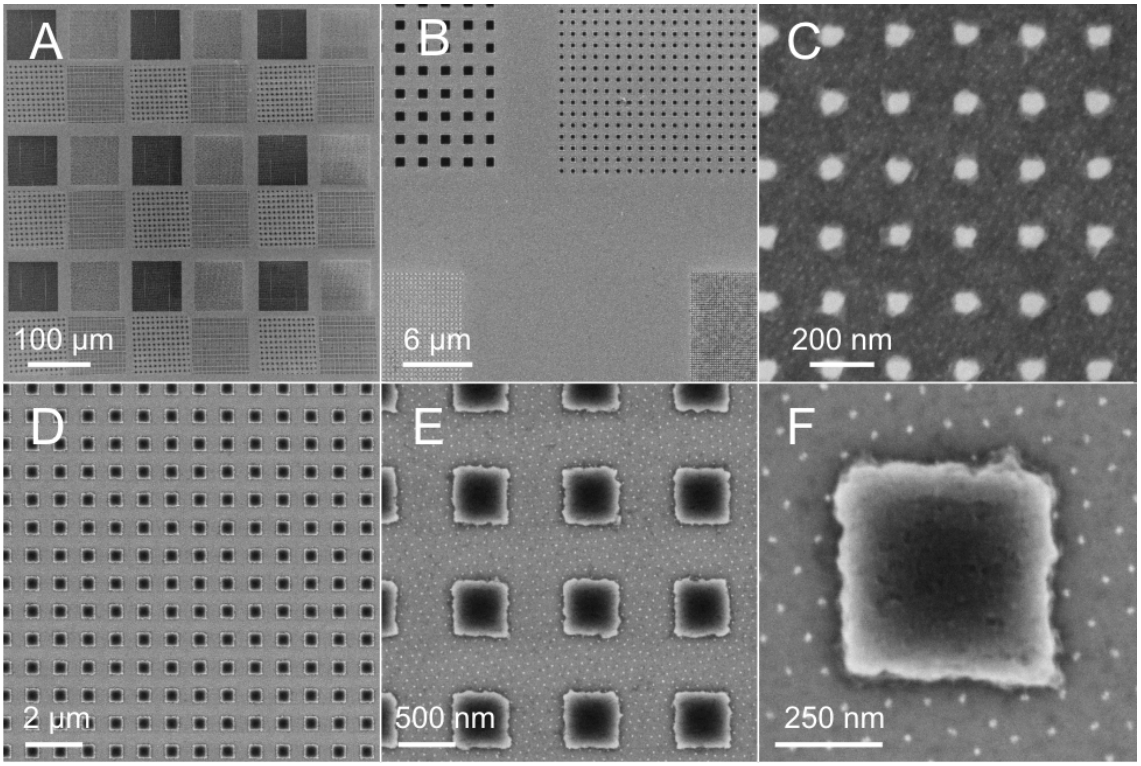

Figure 4.6: (A and B) Overview of the patterns produced by the electron beam lithography with a negative resist. The resist was removed in unexposed parts by development and set free the underlying nanostructure. (C) bright spots depict the accuracy of the lithographic process with resist structures of down to 80 nm in diameter. (D-F) 500 nm sized blocks of exposed resist structures in different magnifications.

to MEBL described in section 4.1. In the case of the micellar resist a dose of 7.5 mC/cm^2 was applied, which compared to 50 $\mu C/cm^2$ in the case of spin coated resist yields a ratio of 1:150. Therefore, the new approach which used a spin coated resist requires only $\frac{1}{150}$ of the applied dose. Neglecting the altering beam current for different exposure processes this would mean that the new approach accomplishes the same pattern size 150 times faster. In other words, one would be able to pattern an area that is 150 times bigger within the same amount of time. An additional fact that leads to even faster exposure times comes into play when the electron beam current during exposure is taken into account. Simplified one can say that, the higher the accelerating voltage chosen for the process the higher is the beam current. With a higher beam current the same dose can be applied in shorter time. Since MEBL is carried out with an accelerating voltage of 1 kV (180 pA), compared to 15 kV (338 pA) for the spincoat resist approach, it can be stated that the time savings using

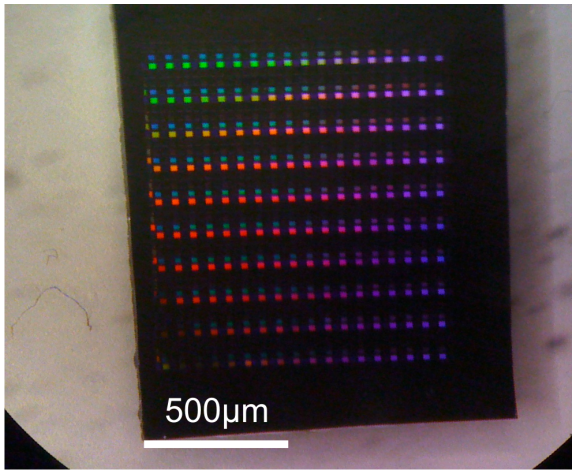

Figure 4.7: Macroscopic overview of micro structure depicted in figure 4.6a and b in detail

the new approach will considerably exceed a factor of 150.* An example of what pattern size can be achieved by an 12 hour exposure is shown in figure 4.7.

The striking improvement in pattern size comes with a number of minor drawbacks linked to this technique. First of all, as seen in figure 4.4 some additional steps are necessary compared to MEBL. This includes applying the resist under clean room conditions. Additionally, the resist is not only sensitive to electron flux but also to light, which requires handling the coated samples in darkness or appropriate (clean room) lighting conditions.

All samples shown in the previous pictures are silicon chips, since electron beam lithography requires conductive substrates. During this work considerable effort has been put into transferring the technique to glass substrates but without noteworthy success. An additional step like coating the sample with a layer of carbon prior to patterning as done for MEBL could not be applied here. This fact unfortunately remains a major drawback and a limiting feature of the technique.

Summarizing it can be said that, with this approach to micro-nano patterning of hexagonal ordered gold particles the the size limits of patterning area have been exceeded manifold compared to the previously used MEBL. It thereby paved the

*Depicted currents were measured at one time point and shall exemplify the relation of accelerating voltage and beam current. These currents are not necessarily linked to a certain accelerating voltage since they are subject to several influences like age of the emission cathode, microscope setup and daily changes, etc. and can vary considerably. Therefore no exact claims have been made on how this fact influences the speed of the process.

way for large area cell adhesion experiments on micro-nano structures. Nevertheless, looking at cell adhesion, the need for largely micro-nanopatterned glass substrates remained, since cell experiments involving fluorescent staining require transparent substrates.

4.3 Electron Flood Gun Lithography

The limit of being only feasible on non-transparent substrates could be overcome by a third method. Hierarchical structuring of block-copolymer nanopatterns was accomplished by cross-linking the polymeric structure via an unfocused electron source instead of exact, guided beam of electrons. This method and the used setup has already been used earlier for lithographic purposes on self assembled monolayers.[76,77] The principle of cross-linking the polymeric structure of block copolymers is the same as for micelle electron beam lithography described in figure 4.1. But the lithographic procedure works in a rather photo-lithographic like manner by exposing the sample through an appropriate mask. Figure 4.8 illustrates the lithographic process.

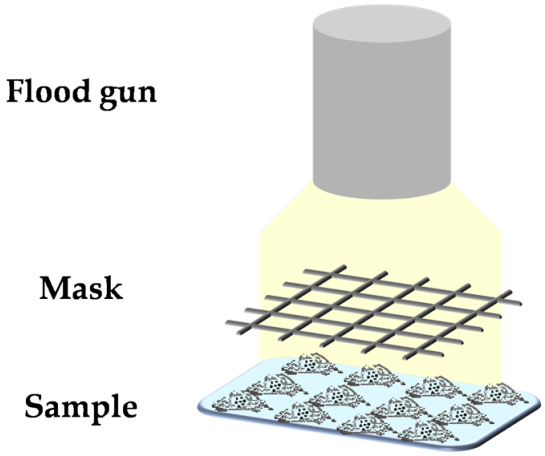

Figure 4.8: Schematic of the flood gun lithographic process. Electrons are emitted from electron flood gun. The structure of the nickel grid, which served as shadow mask was replicated onto the block copolymer coated glass cover slip.

In contrast to photo lithography the mask for the flood gun lithography consists of metal grid. Figure 4.9D shows an SEM image of the nickel grid used for the lithographic process. Polymeric structure in areas, which have been exposed the electronic radiation is cross-linked, whereas non-irradiated areas set free the metal

precursor salt by an ultrasonic treatment in acetone. An additional plasma treatment removes the polymeric debris. The result is a clear replica of the overlying mask in form of a hierarchical gold particle nanopattern. Figure 4.9 shows images of the process steps before (4.9 A - C) and after (E, F) plasma treatment. Up to now

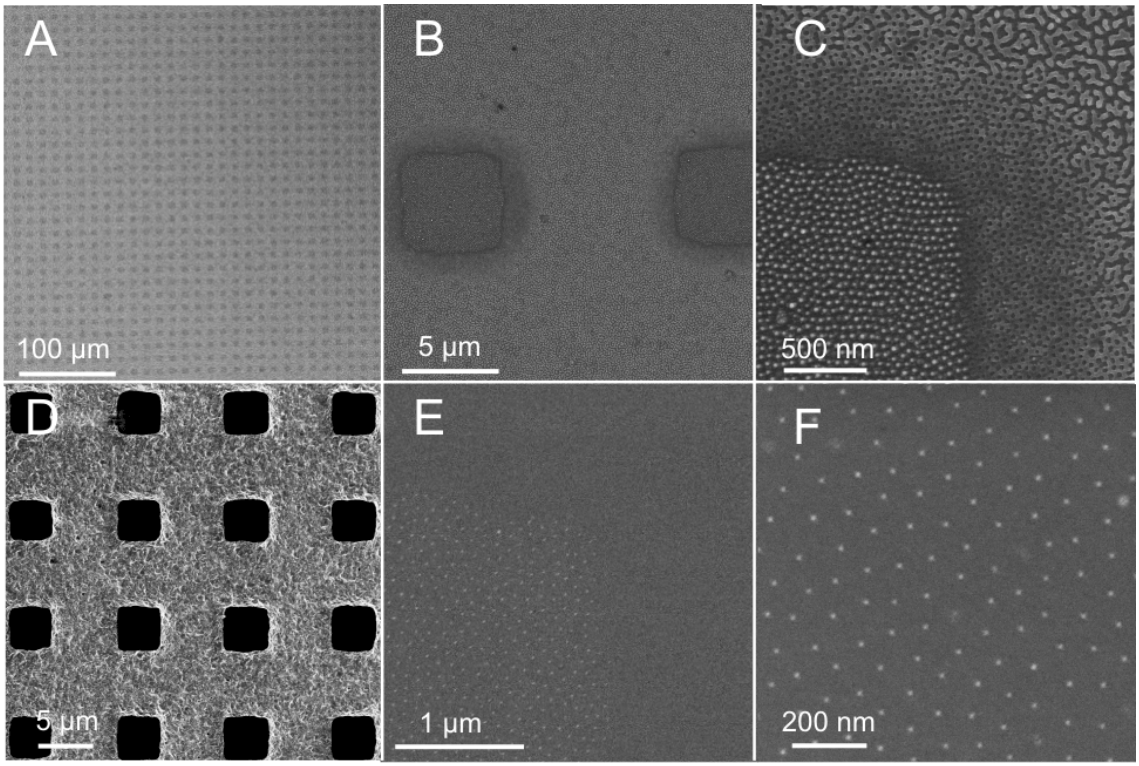

Figure 4.9: SEM Micrographs of the stages in lithographic process executed with an electron flood gun. (A-C) shows the irradiated sample after the ultrasonic lift-off process in different magnification. In the lower left part of (C) indicates polymeric micelles loaded with gold salt that are pinned to the surface. (D) shows the nickel grid which served as lithographic mask for the exposure process. (E and F) shows the micro-nanopattern of gold particles after plasma treatment.

only Ni-grids with a mesh size of 5 μm have been used. Therefore, the resolution limit of this technique cannot be proven to go beyond this limit. However, the sharp edges of the micropattern in images 4.9 B,C and E hold promise for a much higher resolution.

A clear, major advantage of the 'flood gun' technique is the parallel processing. Samples with hierarchical patterns of up to $4cm^2$ could be produced within one exposure step that lasted 10-20 minutes. Additionally, and in contrast to the two other presented methods, the flood gun lithography also works on completely non-

conductive samples. No additional layer of carbon on the sample is required to ensure the working process. The applied electron load is directed away from the sample surface via the conductive Ni-grid and can not cause any unwanted charging effects. Like for any other mask based lithographic process, the presented flood gun lithography has only a reduced flexibility in terms of pattern design. The flexibility depends on commercially available or expensively metal grids. But compared to masks used for photo lithography metal grids are considerably cheaper. The custom made facility allows quick handling of the substrates but because of the experimental setup it is probably difficult to transfer to other locations.

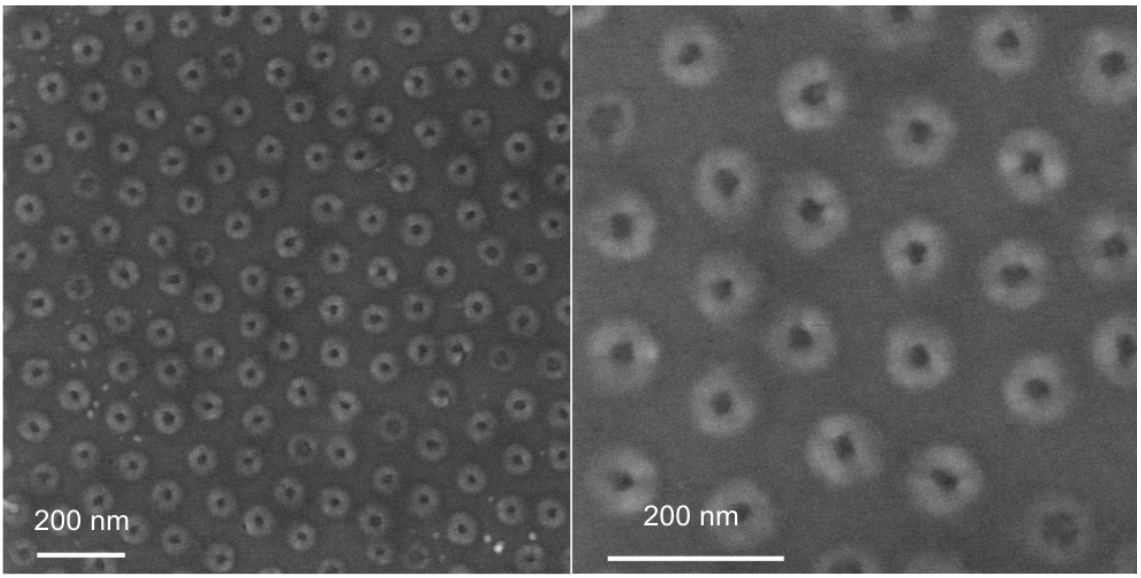

Figure 4.10: SEM micrographs of micellar block copolymer micelles pinned with electrons ejected by the electron flood gun and subsequent treatment with an ultrasonic bath in acetone. With the appropriate dose of electron flux and suitable adjusted ultrasonic intensity polymeric nanopores are formed instead of gold salt loaded micelles. See section 3 for detailed parameters.

A further effect that can easily be generated by flood gun lithography is the generation of polymeric nanopores. See figure 4.10 for detailed images. A similar phenomenon that already has been found previously, described this as "nanohoneycomb" structures.[62] Figure 4.9C already indicates that the intensity of the applied dose determines whether the polymeric resist is cross-linked to an extend that is able to "hold" the metal precursor throughout the ultrasonic treatment step or not. At the edges of the described image a dose bleeding effect can be seen that leads to the generation of a small border of polymeric nanopores around the de-

sired structure. The processes describes so far have been executed with a electron dose of $30mC/cm^2$.† When the applied dose was reduced to $10mC/cm^2$ these pores occurred instead of metal clusters in areas which have been directly exposed to electrons. Higher doses of $50mC/cm^2$ even generated the nanopore structure in "protected" areas under the grid. Figure 4.10 shows examples of this polymeric nanopore structure. In contrast to earlier experiments that have been accomplished by electron beam lithography the flood gun setup is able to produce nano-porous areas of several square centimeters even without a mask if the dose is adjusted correctly.

4.4 Conclusions and Overview

Part I of this work showed three different techniques that are able to hierarchically micro-structure block copolymer derived nanopatterns. The possibilities of micelle electron beam lithography, (sec. 4.1) which already was a known technique, have been extended to arbitrary pattern designs and single particle immobilization. Additionally, two new methods have been developed, which allow for the micro-structuring of larger areas.

	Micellar e-beam	Resist E-beam	Flood Gun	Photo Resist
Accuracy	single particles	$\sim 100nm$	$1-2\mu m$	$\sim 500nm$
Exposed area	$< 1mm^2$	$20mm^2$	whole slide	whole slide
Advantage of technique	arbitrary patterns accuracy	arbitrary patterns large area	non-conductive substrates	non-conductive substrates
Drawback of technique	small area	conductive substrates only	facility	fixed, expensive mask

Table 4.1: Overview over micro-nanostructuring techniques

Another method that shall be mentioned here, which fits in this row of different techniques but was not subject of this work is the "photo-resist approach". Hereby the procedure is very similar to the resist approach shown in section 4.2 but a photo-lithographic exposure step replaces the electron beam exposure step. The main advantage is the transfer of the desired pattern on non-conductive substrates. Table 4.1 shows an overview of available micro-structuring techniques that

†This is the calculated dose for the custom made flood gun setup. This very high value compared to the applied dose in section 4.1 can be attributed to inhomogeneous distribution of the accelerated electrons within the specimen chamber and therefore difficult to compare with dose values described in section 4.1.

are established in the work group so far. It sums up briefly the major advantages and drawbacks of the different techniques, which have already been discussed in the respective chapters.

Summarizing it can be said, that in the first part of this work several ways of hierarchical nanopatterning of block copolymer structures have been developed, that now provide a toolbox out of which a method can be chosen that suits the respective scientific purpose. Possibilities range from single particle deposition to larger scale arbitrary patterns, that can even be designed on non-conductive and transparent substrates. The main application, however, to study protein clustering effects on adherent cells will be subject of part II of this work.

Part II

Cell Behavior on Biofunctional Nanopatterns

Chapter

5

Introduction

5.1 Previous Discoveries

The application of biofunctionalized nanopatterned substrates for cell adhesion studies proved to be a well suited coalition to reach deeper insight in fundamental cellular behavior. Taking advantage of the distinct surface chemistry one is able to control integrin interactions with molecular precision. Spatz and coworkers revealed with the use of these surfaces a clear change of adhesion behavior as a function of lateral spacing of surface-bound biofunctionalized gold nano particles.[50] They were able to prove, that adhesion of 3T3 osteoblasts to these surfaces decreased dramatically, when the lateral spacing of gold particles exceeded a value of 58 nm. The effect did not depend on the overall density of particles on the surface, but rather on local concentrations of c-RGDfK-peptide coated gold clusters. These findings led to the conclusion that local integrin clustering below a lateral spacing of $\sim$60 nm was necessary to induce focal adhesions and to prevent apoptosis. Similar findings were also obtained by other groups but lacked the molecular, nano-scale precision of the nanopatterned substrates used in this work.[49] Figure 5.1 illustrates these findings by showing that intracellular clustering is only possible up to a certain lateral spacing of presented adhesion ligands.

The above mentioned studies underlined the necessity to study adhesion behavior on a precise molecular scale in order to untangle the complexity involved in focal adhesion (FA) formation. Especially studies concerning the existence of hierarchical and cooperative arrangements, and synergistic interactions between focal adhesion proteins, are still poorly characterized. In particular, the significance of the size and

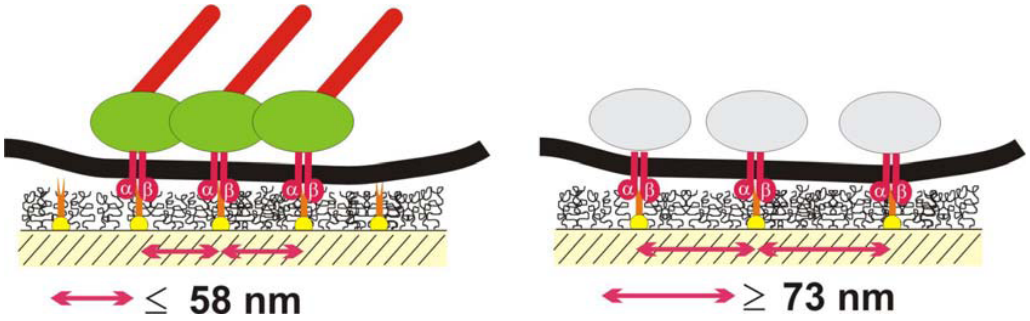

Figure 5.1: Illustration of a cell mambrane that lies on top of a biofuncitonalized nanopatterned surface. The peptides that are bound to the gold particles specifically address only one Integrin dimer per particle. Previous studies showed, that Integrin clustering that is necessary to induce adhesion can be controlled by the underlying particle pattern. Cell were able to adhere on the substrate when particle spacing was 58 *nm* but not if the spacing of 73 *nm* Adapted from [61]

.

shape of FAs for cell signaling, as well as the nano-scale protein topology within these adhesion sites, is not yet understood. This issue will be studied in section 8.1 with rat embryonic fibroblasts.

5.2 The Role of Osteopontin in Allergies

Biofunctional nanopatterns can also serve to study cell-surface interactions in a broader context. The development of allergies for example has been attributed to interaction of dendritic cells with the protein osteopontin. Dendritic cells are a key player in cell mediated immune response as part of the immune system. They reside in peripheral tissues and upon capture of antigens start to migrate towards lymph nodes to act as antigen presenting cells (APC) and induce an immune response. First visualized as Langerhans cells in 1868, dendritic cells (DC) were discovered by Steinman *et al.* in 1973. [78] Since then DCs were found to be the missing link between antigen exposition and immune response. [79,80] DCs undergo different states during their life cycle. Evolving from their respective progenitor cells DCs usually are in an immobile, resting, so called “immature” state, ready to capture antigens in their surrounding. Upon endocytosis of the respective antigen they start to transform to an mature, highly mobile state, in which the processed antigen is presented on the surface via a major histocompatibility complex (MHC) class II surface receptor. The dendritic cell starts to migrate through the lymphatic system to reach lymph

nodes and can thereby act as an antigen presenting cell (APC). T-lymphocytes are then able to recognize the presented antigen as foreign tissue and trigger a specific immune response. Thereby only few DCs are necessary to provoke a strong T-cell response. An overview of the role of DCs is shown in figure 5.2

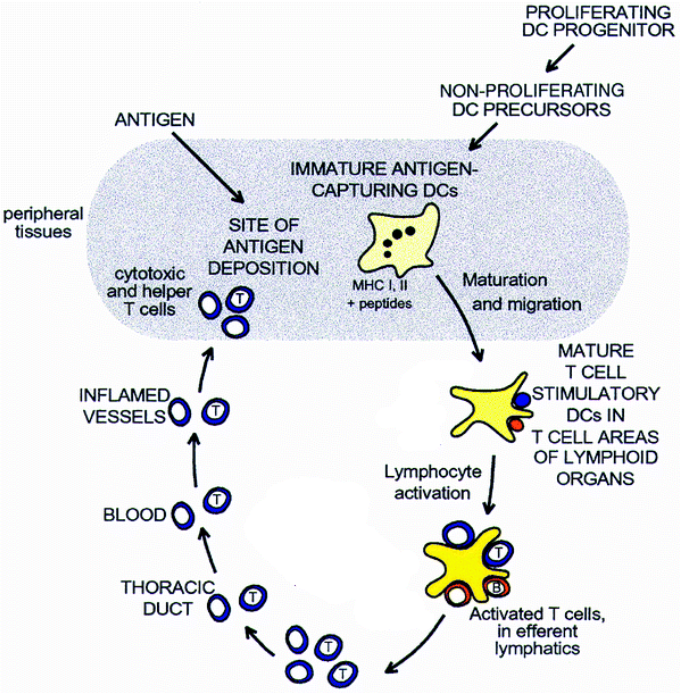

Figure 5.2: Schematic of an *in vivo* immune response. Immature dendritic cells derive from their respective progenitors and as a consequence of antigen uptake start to mature and migrate. Maturation includes the expression of molecules that will lead to binding and stimulation of T-cells in lymphoid tissue. T-cells leaving the lymphoid system trigger an immune response against cells that are presenting the respective antigen. Adapted from [79]

During the maturation process the dendritic cell undergoes several changes in terms of shape and surface protein expression. Figure 5.3 sums up the major differences. Since for example immature DCs bear mainly intracellular MHC II they are hardly able to trigger T-cell immune responses. Additionally, several surface proteins are up-regulated and present in the mature state. These include for example CD54 (ICAM-1), CD58,CD80, CD86, CD40, CD25, IL-12, CD83 and p55, which are mainly responsible for intercellular adhesions and the "communication" with T-cells. Only with the respective proteins on the cell surface a dendritic cell is able to be recognized by a T-cell.

Dendritic cells are also of major importance during development of allergies. Just

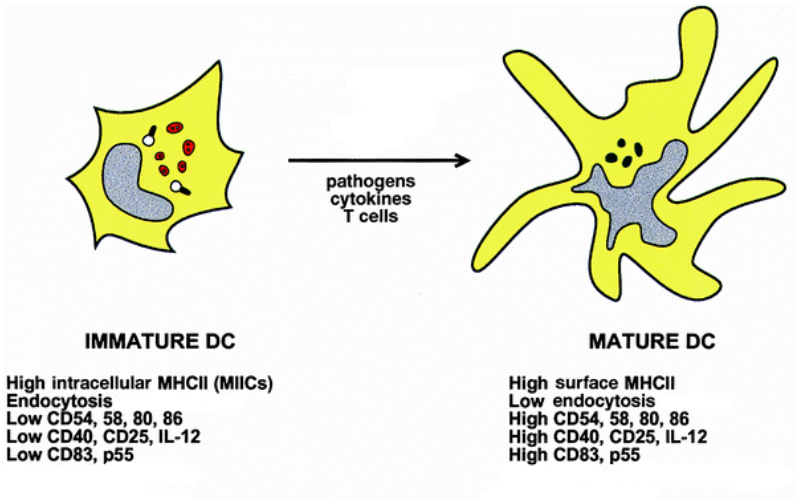

Figure 5.3: Differences between mature and immature dendritic cells. Upon maturation dendritic cells start to express several cell surface receptors that enables them to bind to T-cells and thereby trigger an immune response. Additionally, DCs start to migrate from the peripheral tissues through the lymphoid system to T-cell rich areas in th lymph nodes. Adapted from [79]

like antigens also allergens are processed by DCs and structural information is carried on to trigger an immune response. Through their antigen presenting ability DCs are able to induce an unwanted immune reaction in effector cells against the recognized allergens. A protein that has been reported to be involved in the development of allergic reactions is osteopontin (OPN).[81,82] Osteopontin is a secreted acidic phosphoprotein of differing size (44-75kDa), which is caused by alternative splicing and different phosphorylation and glycosylation patterns resulting in a diverse functionality reaching from bone remodeling, angiogenesis to chemotaxis.[83–85] Osteopontin can bind to extracellular matrix (ECM) components like collagen as well as to cell surface receptors. Notably, a conserved arginine-glycine-aspartate (RGD) sequence of OPN was identified to bind to $\alpha v\beta 5$, $\alpha v\beta 1$ and $\alpha v\beta 3$ integrins.[86] Additionally, osteopontin stimulates cell migration of vascular smooth muscle cells which was shown to be mediated by $\beta 3$ integrins.[87] A very recent piece of the puzzle was added by Xanthou and coworkers stating that OPN plays a crucial role in allergic diseases through the regulation of dendritic cells.[88] They showed, that therapeutic administration of recombinant OPN decreased an established T helper cell type 2 response and protected mice from allergic disease underlining its role as therapeutic target. Moreover, osteopontin controls the migration of dendritic cells towards

lymph nodes. However, the signaling transduction pathways between OPN and DCs and the addressed surface receptors remain unclear.

According to the studies presented above the assumption can be made that an integrin mediated interaction between osteopontin and dendritic cells might bear more than just provide adhesion, but also transmit information that is for example of pro-migratory, activating, polarizing or cell differentiating nature. Biofunctionalized nanopatterns as described in section 6.4 were used in this study to shed light on the interactions of the RGD motif with dendritic cells. With the use of nanostructures it is possible to address single integrins and thereby study spacing dependent cellular integrin clustering on a molecular level or at least provide a defined concentration of surface bound ligands. This study is considered to be a step towards a better understanding of the interplay between dendritic cells and the RGD binding site of osteopontin.

Chapter

6

Theoretical Background

Interactions of living cells and their interactions with the extracellular matrix (ECM) are among the most vital processes in living organisms. Proteins mediating cell-cell and cell-ECM connections are divided in four families of adhesion molecules: Immunoglobulin-cell adhesion molecules (IgCAMs), cadherins, selectins and integrins. However, attachment to an external basement is to a major part mediated by integrins. This anchorage is, apart from few exceptions, vital for cells and precondition in order to proliferate and differentiate. Important parts of these processes and how to mimic essential parts of the ECM for cell adhesion studies will be described in the upcoming sections.

6.1 The Extracellular Matrix

The extracellular matrix provides the physical microenvironment and determines the tissues physical properties, in which cells live. An essential part in the formation of tissues, in which cells are assembled and bound together, is played by the ECM. It is a substrate for cell anchorage and serves as a tissue scaffold, guides cell migration during embryonic development and wound repair, and has other key roles in tissue morphogenesis.[89] Although the understanding of its organization is still incomplete the major components have been well characterized. The whole organization of the ECM is determined by fibroblasts, which segregate these components. But also, interdependently, cell organization relies on structural integrity of its surrounding.

Large amounts of space are consumed by glycosaminoglycans (GAG) which can simply be considered as unbranched polysacharide chains. If linked to a protein

they are called proteoglycans. The GAG side chains of proteoglycans have the ability to form gels of varying pore size and charge density which regulate the traffic of molecules or cells according to their charge or size. But also a major role in chemical signaling between cells is attributed to proteoglycans.[90] See figure 6.1 for an illustration of the ECM and a cross section of a cell membrane.

The most abundant protein in mammals and also a major constituent part of the ECM is collagen. Built out of stiff triple helices mainly consisting of Glycin and Prolin it serves as a mechanical basement. Depending on the type of collagen and its organization it can serve as structural basis of bone, cartilage or next to cells serve as a fine mechanical network resisting tensile stress. A molecule that was found to establish a firm connection between the mechanical basis of the ECM and cells is fibronectin, which is a dimer composed out of two large subunits that are joined together by disulfide bonds. Each monomer exhibits binding sites for self-association, collagen, heparin and cell binding. Cell binding is established via the short peptide sequence RGD.[91] This important sequence provides attachment sites for integrins that are cellular mediator for adhesion.

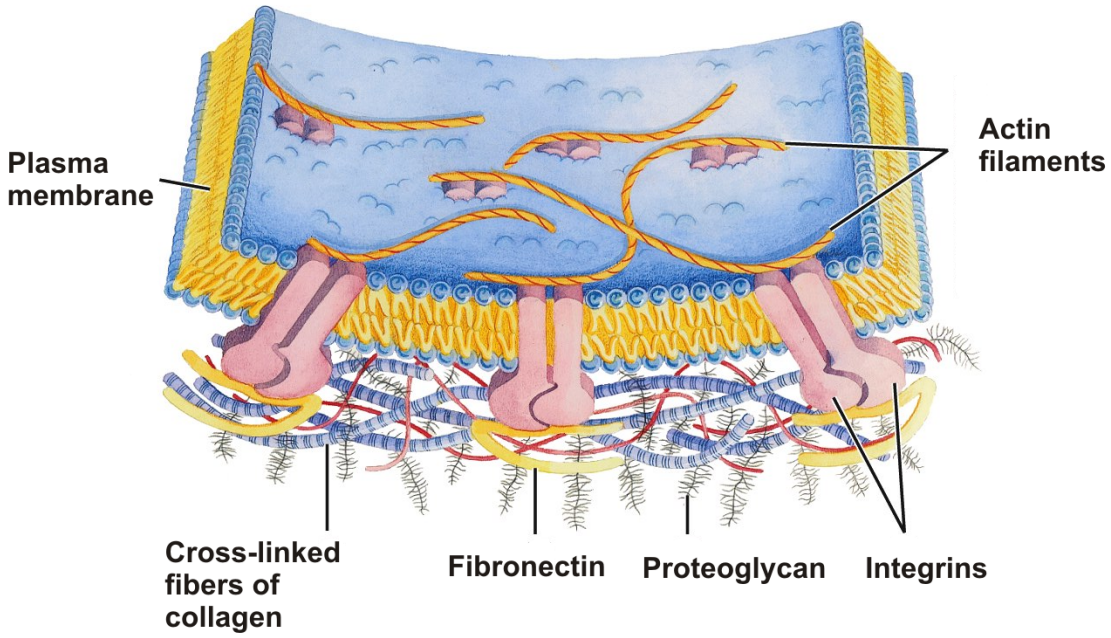

Figure 6.1: Illustration of organization and composition of the extracellular matrix. Courtesy of J. Robertus, Insitute for Cellular & Molecular Biology, Uniersity of Texas, Austin, USA.

6.2 Integrins

Living cells use several different ways to get in contact with their surroundings. The attachment to other cell membranes or external substrates requires distinct interactions of transmembrane proteins with the ECM or other transmembrane receptors of neighboring cells. This is achieved by establishing a link between extracellular and cytoplasmic entities. The connection is not only mechanical linkage but also provides a bidirectional flow of information.

Parts of this work focus on the adhesion of cells to external substrates which is mediated by the integrin receptor family.[92] Integrins are only expressed in metazoa and consist of a heterodimer which is divided in the so called α- and a β-subunit. A major part of each subunit of about more than 1600 amino acids protrudes the extracellular space but bears only a short cytoplasmic domain of 20-50 amino acids.[93] Figure 6.2 shows a schematic drawing of such dimers. Integrins are considered to be able to switch between an activated (extended) and an inactivated (bent) state. Connection to external ligands is only possible in the activated state. Integrins rest in a bended inactivated state on the cell surface. Upon activation by internal or external stimulus they "open up" and extend the extracellular domain. However, the details of the activation progress are still disputed. A switch-blade or flick-knife motion for the opening process was proposed by Beglova *et al.*[94] opposing the angle-poise model by Armulik and coworkers.[95] The opening up to the activated state also enables homomeric interactions between integrin subunits. This homomeric affinity leads to oligomerization and clustering of integrins. Lin and coworkers have shown that this clustering has strong influence on the binding affinity of intergrins towards fibronectin fibers. By introducing mutants of integrin subunits that only have small (1-2 kcal/mol) enhanced affinity towards each other an fivefold amount of fibrinogen was bound compared to wildtype integrins.[96,97] These mutants also induced homo-oligomerization *in vitro* and constitutive integrin activation and clustering *in vivo*. This strongly suggested a causal connection between integrin clustering and integrin activation. The fact that integrin clustering is of major importance for establishing cell adhesion has been shown recently and will also be subject of this work.[61]

Combinations of different α- and β-subunits yield different integrins with specific affinity to certain recognition sequences. Early evolutionary stages provided only 2 different integrins which, according to the current knowledge, branched out since then to a wide variety of 24 different combinations of α- and β-subunits.[93] An

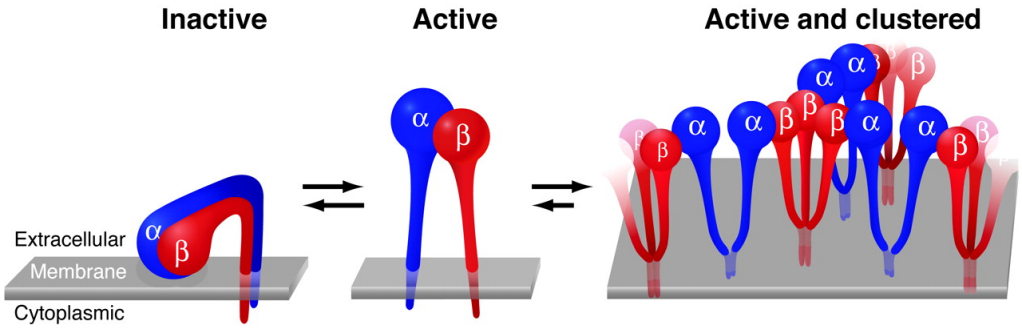

Figure 6.2: Activation process of the integrin $\alpha - \beta$ heterodimer. The bent (inactive) integrin opens up and extends its extracellular domain to an active conformational state. The extended (activated) conformation enables oligomerization of similar subunits which leads to integrins clustering. Adapted from [96]

overview of what now is called the integrin receptor family is shown in figure 6.3. A very prominent recognition sequence is the tripeptide arginine-gylcine-aspartic acid (RGD). (Figure 6.6) This sequence is ubiquitously expressed in different proteins of the ECM like fibronectin or vitronectin. Other subfamilies of integrins specifically bind to e.g. laminin or collagen. It was not until Xiong *et al.* shed light on the understanding of structure and function relations by revealing the crystal structure of αv β3 integrin with its RGD ligand that led to a deeper understanding of the recognition process. [98,99]

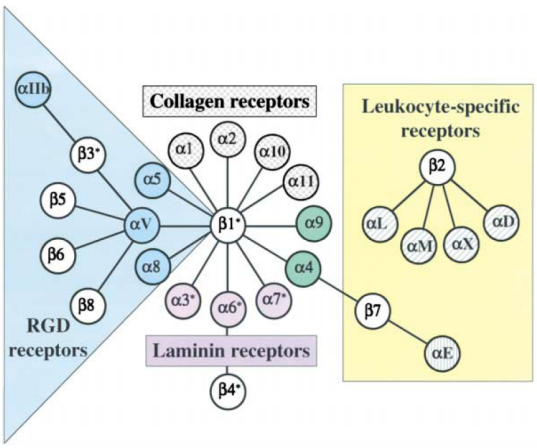

Figure 6.3: The integrins receptor family. Different α- and β-subunits of the Integrin Heterodimer yield different receptors that specifically address different recognition motifs. Adpated from [93]

As mentioned above, integrins connect both the ECM and the internal skeleton

of the cell by forming stable contacts that are the basis for cell proliferation and differentiation. Integrins build up a mechanical connection between the ECM proteins and the actin cortex. Via this connection a cell can actually "hold" itself onto an external substrate and even apply mechanical force. Other than the direct external adhesion to the respective ECM protein, internal anchorage is predominantly of indirect nature. After binding to their external ligands, integrins connect via the cytoplasmic domain of the β-unit to intracellular anchor proteins like talin, α-actinin and filamin. These anchor proteins in turn can bind directly to the actin cortex of the cell or other anchor proteins like vinculin. This connection mediates mechanical stress and provides adhesion but thereby also activates several intracellular signaling cascades. An overview of proteins and signaling pathways that are involved in integrin mediated adhesion processes is shown in figure 6.4. Cell adhesion thus has influences on proliferation, survival/apoptosis, shape, polarity, motility, gene expression, and differentiation. Therefore integrin mediated cell adhesion can be termed a vital process that is important for cell survival.[100,101] The importance of integrins is underlined by several studies in which different integrin knock-out mice show phenotypes ranging from complete block in preimplantation development[102] (β1) over major developmental defects (α4, α5, αv, β8)[103–105] up to perinatal lethality (α3, α6, α8, αv, β4, β8)[106,107] and several others.[93] In general it can be said, that integrin mediated signals are necessary in normal cells to block apoptosis and to stimulate cell cycle progression and therefore vital signaling processes.

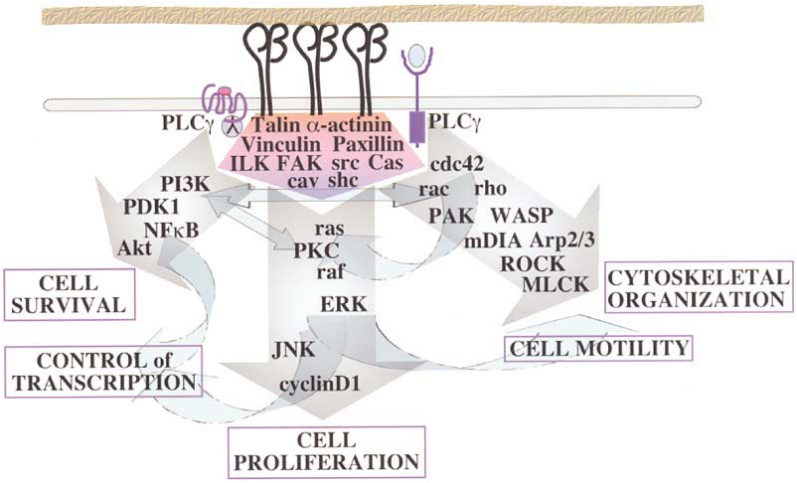

Figure 6.4: Upon activation of integrins several signaling cascades are triggered. The pathways range from cell survival to cytoskeletal organization. Adapted from[93]

Figure 6.4 already indicates, that integrin clustering mechanisms are only the "tip of the iceberg" in terms of signaling cascades and proteins that are involved in mediating cell adhesion. A great number of proteins that stand in interdependent, complex relations to each other are involved in building up structures that have been termed focal adhesion. These so called focal adhesion will described in the following section.

6.3 Focal Adhesions

Upon adhesion to an external substrate the mediating integrins build up cytoplasmic connections to several proteins that establish a firm link to the actin cortex of the cell and/or trigger signaling pathways which include vital intracellular mechanisms as described in section 6.2 and figure 6.4. Integrin induced conglomeration of proteins around the cytoplasmic integrin domains have been termed focal adhesions.[89] Focal adhesions are flat, elongated structures that are several square microns in area, and are often located near the periphery of cells[108,109] A distinction is drawn between variants of focal adhesions that have been termed focal complexes, fibrillar adhesions and podosomes. However, the categorization is mainly due to morphological qualitative features, since the functional differences are still poorly understood. See table 6.1 for an overview on different adhesion types.

Property / Structure	Focal complexes	Focal adhesions	Fibrillar adhesions
Location	Edge of lamellipodium	Cell periphery	Central region of cells
Morphology	Dot-like	Elongated, oval	Fibrillar beaded
Size (long axis)	$1\mu m$	$2-5\mu m$	$1-10\mu m$
Typical constituents	Paxillin Vinculin Tyrosine-phosphorylated proteins	αv integrin Paxillin Vinculin α-actinin Talin Focal adhesion kinase Tyrosine-phosphorylated proteins	α5 integrin Tensin

Table 6.1: Charcteristic features of different types of cell-matrix adhesions. Adapted from[89]

The fact that focal adhesions are still poorly understood is not due to a lack of

research in that field, but is rather contributed to the mere impenetrable complexity of the system.[109] Figure 6.4 and 6.5 give an impression on how many proteins are involved in building up focal adhesions and the interdependence of different signaling pathways. Most common integrins that are associated with focal adhesions are $\alpha v\beta 3$ (fibronectin) and $\alpha 5\beta 1$ (vitronectin). A major initiator of focal adhesion seems to be externally applied local mechanical force,[110] but also integrin clustering by itself can induce various signaling events.[111] Initial stages of focal adhesion building include so called microspikes.[112] Spikes or microspikes are 210 μm long, unbranched projections of the cell surface and are built of a core bundle of F-actin and contain fascin.

There is no clearly defined progress of evolutionary stages in focal adhesions, but build up of cellular attachment sites usually involves focal complexes, which are rather small (see table 6.1) and can be of transient nature, or evolve to mature focal adhesions or even fibrillar adhesions. However, the definition of these different adhesion types is not very distinct and transitions between different states are rather blurry than exactly defined. (See table 6.1) Nonetheless, several main steps are known for the subsequent maturation of focal adhesion to firm fibrillar adhesions. The maturation process is considered to be an interplay of external triggers and cellular response events. The major part of which has proven to be involved in transduction of local mechanical force from the ECM to the cytoskeleton.[89] However, the generation of focal adhesion plaques are a result of the precedent clustering of integrins which is the basis of formation of proper adhesion sites.

6.4 Biofunctionalization

Substrates produced by BCML are coated with an array of particles arranged in a quasi hexagonal pattern. This array has proven to be a perfect means for studying cellular behavior by functionalizing this pattern with molecules that provide biological information to the attaching cell. The very prominent integrin recognition sequence RDG can be synthesized chemically and bound covalently to gold particles on the surface via a thiol group that is part of the RGD peptide.[113] This surface bound peptide is mimicing an ECM that provides anchor sites to cells at exactly defined spots. The peptide used throughout this work is a special cyclic-RGDfK peptide (f=**D**-phenylalanine) which has shown to have high affinity and specifity

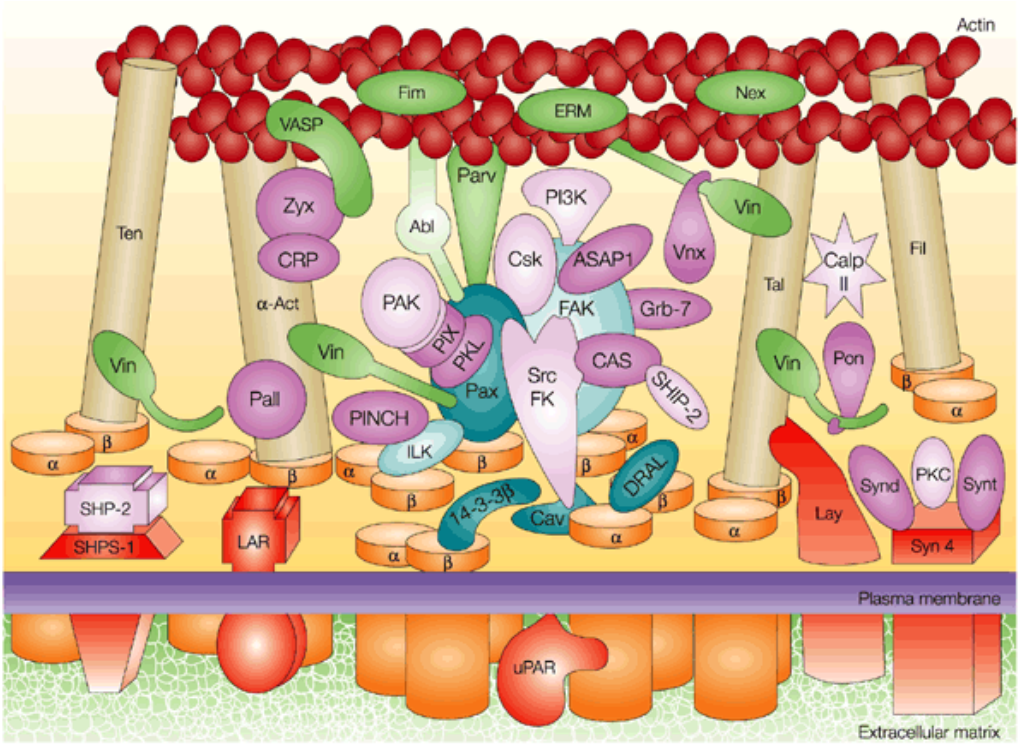

Figure 6.5: Schematic of focal adhesion associated proteins and structures. Primary adhesion receptors are the integrins shown as orange cylinders at the bottom. Only the four components α-actinin (α-Act), talin (Tal), tensin (Ten) and filamin (Fil), shown as golden rods establish a direct connection of integrins to the actin cortex of the cell. Proteins shown in blue are integrin-associated and therefore closer to the cell membrane. These include focal adhesion kinase (FAK), paxillin (Pax) integrin linked kinase (ILK) down-regulated in rhabdomyosarcoma LIM protein (DRAL), 14-3-3β and caveolin (Cav). Other membrane associated proteins are shown in red. Actin-associated proteins (green) include vasodilator-stimulated phosphoprotein (VASP), fimbrin (Fim), ezrinradixinmoesin proteins (ERM), Abl kinase, nexillin (Nex), parvin/actopaxin (Parv) and vinculin (Vin). Other proteins that are of minor importance for this work are shown in purple. Adapted from [89]

towards αvβ3 and αvβ5 integrins.[114] See figure 6.6 for the chemical structure of the peptide.

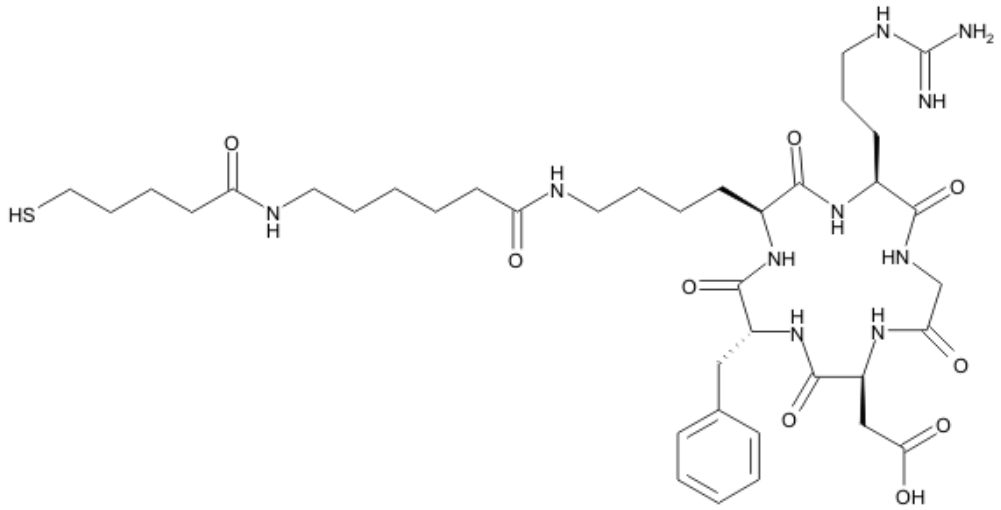

Figure 6.6: Chemical structure of a cyclic RGDfK Peptide with a thiol group that is able to covalently bind to gold particles. The bound peptide mimics parts of the ECM and thereby provides anchor points for cells. The molecule was kindly provided by the group of Prof. Kessler. See section 7 for details.

However, to ensure that cell-surface interactions are confined to bio-functionalized gold particles, the area in between needs to be made unaccessible for cells. A substance which has proven to be useful to inhibit cell-surface interactions is poly(ethylene glycol) (PEG). PEG-derived materials are generally considered to be particularly effective candidates for the fabrication of protein-resistant materials.[115] Its capabilities in protein repellency, inhibition of unspecific interactions and bio-compatibility are known and widely used.[116–118] If those protein repellent properties shall be transferred to the silicon or silicon dioxide surface around the gold particles of nanopatterned substrates an electrostatic or covalent linkage is necessary. A prominent example of electrostatic linkage is the use of poly(L-lysine)-g-poly(ethylene glycol) (PLL-g-PEG). The adsorbed layer of copolymer is thought to form a comb-like structure at the surface, with positively charged primary amine groups of the PLL bound to the negatively charged substrate, while the hydrophilic and uncharged PEG side chains are exposed to the solution phase and provide protein resistance.[115] An extensive study on different PEG derivates that can be covalently bound to sil-

icon or silicondioxide surfaces revealed, that m-PEG2000-urea (Figure 6.7) was the best choice for inhibiting cell adhesion whilst still providing enough space for surface bound bio-functionalized particles to access cellular receptors (or vice versa).[119] An additional advantage of covalent linkage is the long term stability. Even under cell culture conditions this "passivating" PEG layer conserves its protein repellent properties for up to seven days.

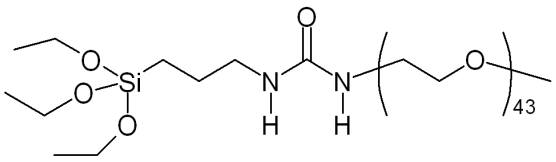

Figure 6.7: Chemical structure of m-PEG2000-urea which is used to "passivate" the interparticle area on the nanopatterned surface.

The combination of both above described techniques; the linkage of c-RGDfK-thiol to gold nano particles and the linkage of m-PEG-urea via a silane bond to the glass surface, generates a powerful tool to investigate cell adhesion behavior on a molecular level. A schematic of the biofunctionalization process is shown in figure 6.8. Even though possibly several c-RGDfK-thiol molecules bind to one gold particle the size of the attaching integrin dimer is $\sim 10\ nm$ and it therefore appears reasonable to claim that one integrin dimer is only able to interact with one gold particle at a time.[98,99]

Binding of peptides to gold surfaces was analysed by quartz crystal micro balance (QCM). Figure 6.9 shows the binding of cyclic-RGDfK-thiol to gold. The frequency drop at addition of peptide and the fast saturation clearly indicate that the binding step is completed after $\sim 20\ min$. Thus, the former protocol for functionalization has been modified from 4h incubation time to now 45 minutes.

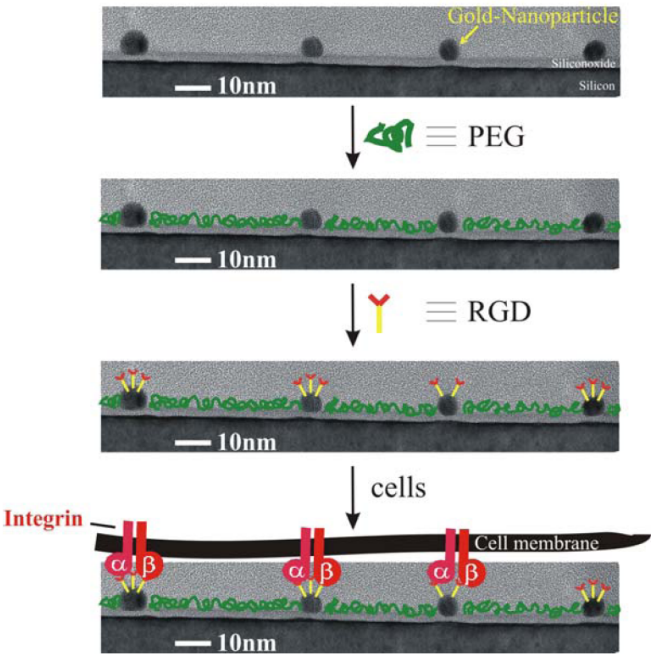

Figure 6.8: Biofunctionalization scheme for nanopatterned surfaces. In a first step PEG is covalently bound to the glass or silicon surface preventing unspecific interactions. Secondly c-RGDfK-thiol is coupled to the gold particles which then provide single integrin attachment sites. [61]

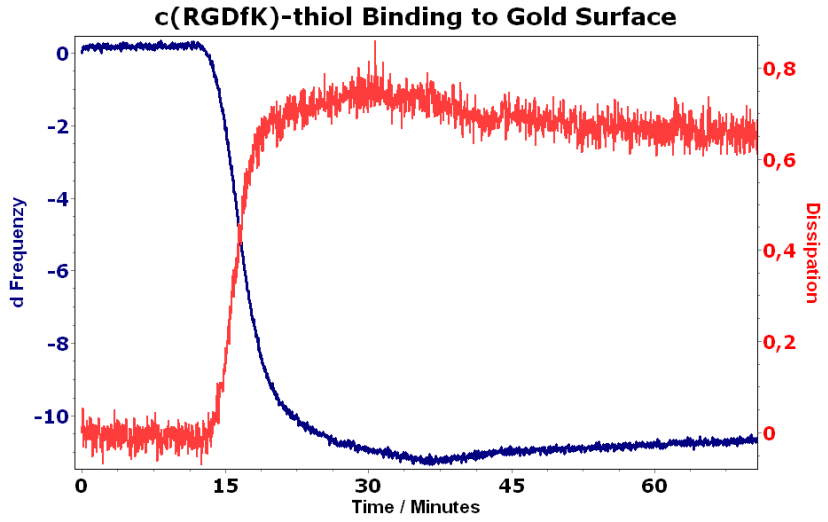

Figure 6.9: Quartz crystal micro balance measurement of c-RGDfK-thiol binding to a gold surface. Frequency drop indicates binding of the peptide.

Chapter

7

Materials and Methods

Cell Handling REF52 (rat embryonic fibroblast) cells expressing yellow fluorescent protein (YFP)-paxillin fusion proteins (kindly provided by Prof. B. Geiger, Weizmann Institute of Science, Rehovot, Israel) were maintained in DMEM supplemented with 10% FBS and 1% L-glutamin (Invitrogen GmbH, Karslruhe, Germany) at 37°C and 5% CO_2. After the cells reached confluence, they were first rinsed with sterile PBS (Gibco-BRL, Karlsruhe, Germany) and then released from the support by incubating the cell culture with a trypsin-EDTA 2.5% solution (Gibco) for 3 min. For adhesion studies, cells in the culture were trypsinized in 2.5% trypsin-EDTA and plated on the surfaces in DMEM containing 1% FBS and 1% antibiotics. For microscopy and imaging experiments, cell plating density was 500 - 900 $cells/mm^2$.

Extraction of Dendritic Cells Murine dendritic cells were extracted from bone marrow.[120] Mice (C57/Black 6, age: $\sim$ 6 weeks) were killed by cervical dislocation. Tibia and femur were obtained and stored under sterile conditions on ice. Bones were washed in 70% Ethaonol and PBS for $1min$. Epiphysises were truncated and bone marrow was washed out with sterile PBS using a syringe. The cell suspension was filled up with RPMI-1640 cell culture medium. After a centrifugation step (5 min, 230 g, 4°C) the cell pellet was resuspended in RPMI medium supplented with GM-CSF (40 ng/ml) and IL-4 (10 ng/ml) (PeproTech GmbH, Hamburg, Germany) and distributed over two 24-microwell plates. At day 3 after extraction half of the medium was exchanged with newly added cytokines.

Cells were harvested at day 5 by density gradient centrifugation or magnetic beads. For purification via the Nycodenz method cells were carefully resuspended and transferred to 15 ml falcon tubes in 8 ml portions. $2ml$ of Nycodenz (Axis-shield, Oslo, Norway) were carefully added at the bottom of the cell suspension and centrifuged (600, 20 min, 21°C). The middle layer was washed in PBS ($4°C$) and centrifuged again (230 g, 5 min, 4°C). The last step was repeated and cells were cultured ($1 \times 10^6/ml$) RPMI medium supplemented with GM-CSF (40 ng/ml) and IL-4 (10 ng/ml) at 37°C and 5% CO_2. Additionally, cells were purified using magnetic beads via Magnetic Cell Sorting of Human Leukocytes (MACS). MACS buffer: 500 ml PBS was supplemented with 0.5% BSA (Sigma) or 1% FCS (PAA Laboratories GmbH, Pasching, Austria) and 2mM EDTA. The sulotion was filtered through 0.2 μm pores to reach sterility at 4 °C and degased before use by ultrasonic treatment. Human DCs: Buffy coat was diluted to a total volume of 180 ml or in case of fresh blood 1:1 with PBS. 30 ml of diluted cell suspension was added to 15 ml Lymphoprep (PAA Laboratories GmbH, Pasching, Austria) in a 50 ml Falcon tube. The tube was centrifuged at 400 g for 25 min at 21°C with weak acceleration and brake. The white interphase was taken up in PBS and centrifuged at 1200 RPM for $10min$ and the supernatant was discarded. 10 μl MACS microbeads (CD14, CD11c or MHCII) and 90 μl MACS buffer were added per 1×10^7 cells to the suspension. MACS columns were incubated with MACS buffer at 4 °C before cell suspension was added to the column wich is attached to the magnet. After 3×3 ml of washing the column with MACS buffer magnet was removed and beads were eluted with 5 ml MACS buffer. The Eluate was centrifuged and cells were cultured under above described conditions.

Extracted dendritic cells were cultured in RPMI 1640 medium supplemented with 10 % FCS PAA, 1% L/G, 1% Pennicilin/Streptomycin, 1% non essential amino acids, 2.5% HEPES buffer, GM-CSF (40 ng/ml) and IL-4 (10 ng/ml).

Critical Point Drying Cultured cells adherent to nanostructured surfaces were fixated with a 37°C solution of 4% paraformaldehyde (PFA) or 4% glutaraldahyede (sigma-Aldrich) in PBS for 20 min. The fixation solution was exchanged with PBS and shortly therafter washed with water/ethanole mixtures of increasing ethanole proportions. Beginning with 50% and followed by 70%, 80%, 90% and three times 100% ethanol. Each incubation step was at least 30 min. The samples were trans-

ferred to a critical point dryer (CPD 030, BAL-TEC AG, Liechtenstein / Leica Microsystems, Wetzlar, Germany) that was filled with ethanol. The intermediate agent was exchanged with liqud CO_2 at 10°C by several filling and draining steps. Critical point was reached by heating the chamber to 40°C which yielded a chamber pressure of $\sim$ 80 bar. Presure was released slowly whilst mainting a chamber temperature of 40°C through constant heating. Afterwards, samples were directly coated with a layer of carbon to achieve conductivity.

Staining and Image Acquisition Fixated cells the following washing steps: 2 $\times$ with PBS, 1 $\times$ with 0.1% Triton X-100 in PBS for 5 *min* and 2 $\times$ with 0.5% BSA in PBS for 5 *min*. Then samples were placed on top of a drop (50-70 μl) of Phalloidin-TRITC (1:100) and incubated for 1h at RT. Samples were again washed with 3$\times$ with 0.1% Tween20 in PBS for 10 *min*. Samples were mounted with Mowiol on standard microscopy slides and dried at RT. Fluorescent images were taken with a DeltaVision imaging System from Applied Precision, Issaquah, Washington, USA. Objective: Olympus 60$\times$/1,42 PlanApo N oil immersion. Critical point dried cells were imaged with a scanning electron microscope (Zeiss Ultra 55, Zeiss, Oberkochen, Germany)

Flow Cytometry Cells were harvested be resuspending, washed with PBS twice and centrifuged at 300 *g* for 5 *min*. 1 μl of antibodies against CD11c (Biotin Hamster Anti-Mouse BD Cat. No 553800 lot 85225) or CD 44 (Biotin anti mouse (Pgp-1, Ly 24) (IM7), Cat no. 553132, Lot 11555) (1 μl per 1 million cells) was incubated for 20 min in darkness at RT. After a subsequent washing step as described above 0.5 μl of fluorescently labeled streptavidin (BD PE Cy5 Streptavidin Cat 554062 Lot 84570) was incubated for 20 *min* at RT. Integrins were labeled directly (beta3) (CD61) by FITC anti-mouse rat CD61 Cat No. 104305 or indirectly (Alphav) (CD51) purified BD, Cat No 552299 + goat anti rabbit PE labeled (PE goat anti rat BD Cat 550767, Lot 91686). Flow cytometer was a Facs Calibur by BD Biosciences, Franklin Lakes, NJ, USA.

Biofunctionalization Glass cover slips or cut silicon chips bearing the nanostructure were activated for 5 min by plasma etching at 0.5 *mbar* H_2 and 150 W. Samples were immersed in a modified Schlenck flask under inert conditions with enough dry toluene to cover all sample surfaces. After adding 200 μl of triethylamine (Sigma-

Aldrich) and 3 mg of custom made poly(ethylene glycol) (mPEG2000-urea)[119] the tightly closed flask was heated to 80°C for 15h. Samples were rinsed in ethyl acetate and methanol and blow dried under a stream of nitrogen. Samples were used directly after passivation and placed on top of a 20 μl drop of 25 μM cyclic-RGDfK-thiol peptide solution for 45min. Cyclic-RGDfK-thiol peptide was kindly provided by the group of Prof. Kessler.* See figure 6.6 for a detailed molecular structure. Samples were washed extensively with ultrapure water for a minimum of 4h on a shaker whilst exchanging the water 6 times.

*Prof. Kessler, Institute for Advanced Study, Department Chemie, TU München, Lichtenbergstr. 4, D-85747 Garching

Chapter

8

Results and Discussion

8.1 Rat Embryonic Fibroblasts

In order to study these focal adhesion associated protein organization rat embryonic fibroblasts, that have been stably transfected to express yellow fluorescent protein (YFP) that is fused to paxillin in the living organism (REF52-YFP-Pax), were seeded on biofunctionalized micro-nanopatterns as described in section 4. Paxillin, as a central part of FAs (See figure 6.5 on page 58) resides very close to the cell membrane and possibly establishes direct association β-integrin tails or through an intermediate protein.[121] These cells have already been used in previous studies to give insight on focal adhesion dynamics.[122] Fluorescent images of adherent REF52-YFP-pax cells therefore give insight in the basal shape of a focal adhesion. Parts of this work have already been published before,[61] but the additional data on this topic completes the view on paxillin domains linked to focal adhesion formation on hierarchical nanopatterns.

On the other hand fluorescent images are limited in their resolution to the emitted wavelength and therefore can provide information on colocalization of proteins but lack the molecular details to resolve single protein interactions. Thus, adherent cells were also imaged by SEM. Figure 8.1 exemplifies the adhesion behavior of REF52-YFP-Pax cells on biofunctionalized micro-nanopatterns. A rat embryonic fribroblast was cultured for 3 h under the earlier described conditions (section 7, page 63) on a micro-nanopattern. Clearly to see, cell adhesion is limited to areas of biofunctionalized particles and cell morphology is aligned according to the underlying pattern. Additionally, cell-surface interactions only occur at the particles

and not at the area in between. Compared to patterns produced in section 4.2 the order parameter of the particles seems to have diminished considerably. In fact, the slightly chaotic appearance of the pattern derives from additional cellular material secreted by fibroblasts in general and can also be attributed to several washing steps during the preparation process, but have no effect on cell surface interactions.

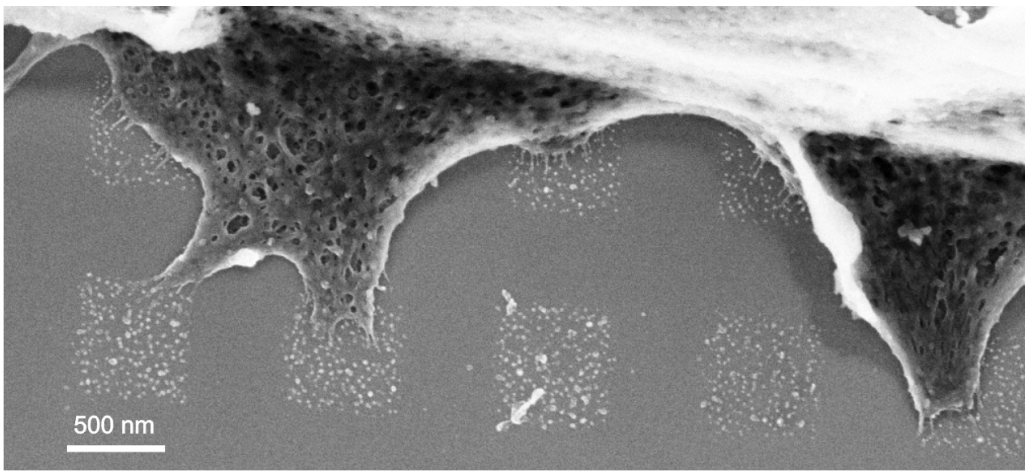

Figure 8.1: SEM image of REF52-YFP-Pax cells adherent to a micro nanostructure of biofunctionalized gold particles on a silicon surface. Cells were fixated and critical point dried after 3 hours of culturing on the surface. Cell morphology shows a clear alignment according to the underlying pattern. Cell-surface interactions only occur at biofunctionalized particles.

during this work an extended study on adhesion behavior was accomplished by producing micro-nanopatterns with squared adhesive patches of 100 nm, 250 nm, 500 nm, 1000 nm and 3000 nm edge length separated by the same distance as exemplified in figure 4.6 D-F on page 36. All patterns were biofunctionalized with c-RGDfK-thiol according to section 6.4.

The patterns comprised defined numbers of functional particles ranging from ~ 6 to ~ 3000 per individual square. The lateral spacing of the particles in all patterns was kept constant at 58 nm. See figure 8.2 and table 8.1 for details. Since this particle densitiy is only localized at certain spots it does not represent the overall densitiy of particles on the surface. Thus, the local spacing of 58 nm equals a "global" density of 116 nm spacing for all presented micro-nanopatterns according to equation 2.4 on page 18. Adherent cells were visualized by fluorescence microscopy and by SEM. Fluorescence microscopy included visualization of paxillin via the cell-expressed YFP and actin via staining with Phalloidin-TRITC. Fluorescent images

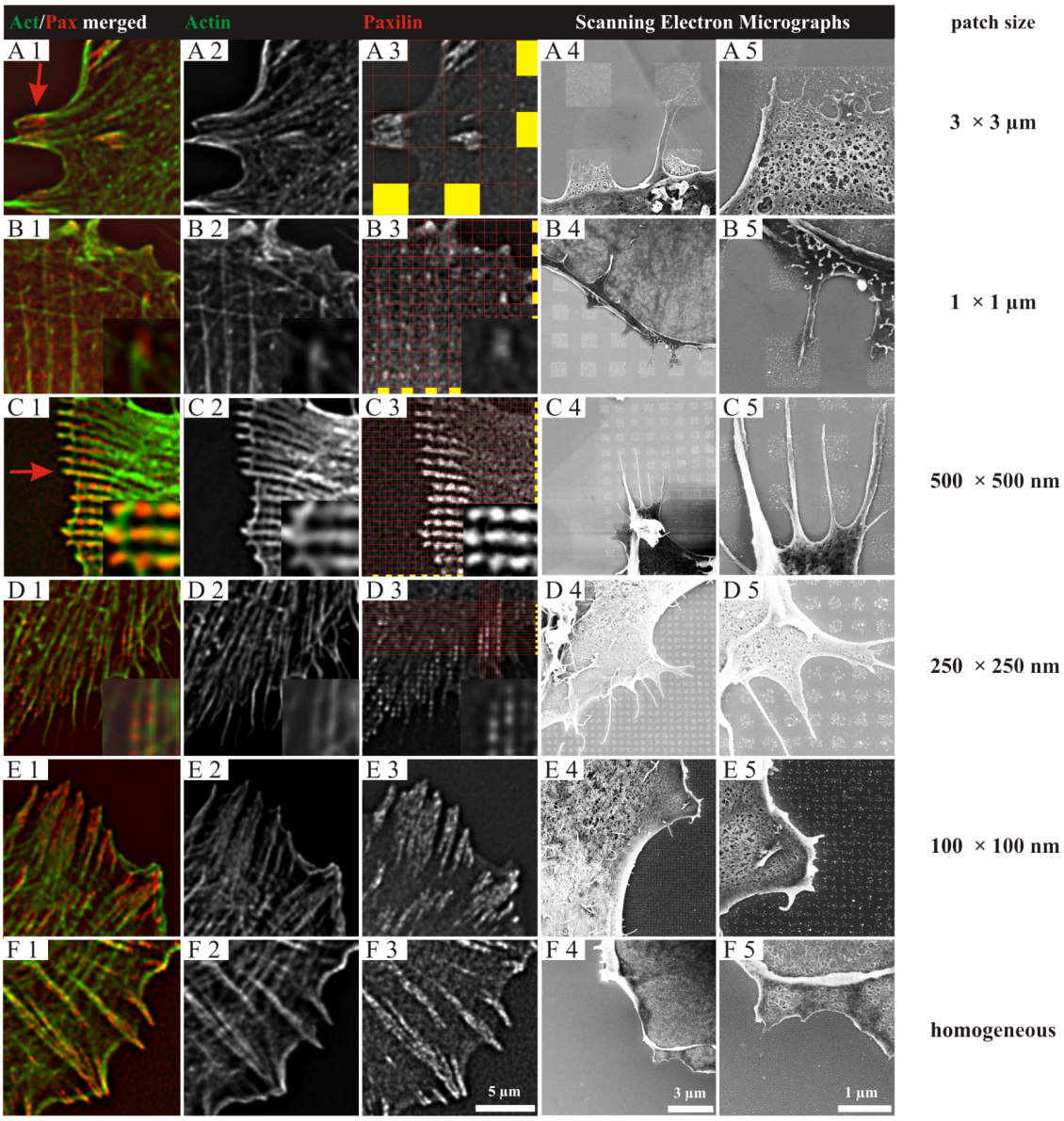

Figure 8.2: Close-ups of FA and cytoskeleton formation of REF52-YFP-Pax cells plated for 3 h on hierarchically structured nanopatterns. Side lengths of squares: 3000 Fnm (row A), 1000 nm (row B), 500 nm (row C), 250 nm (row D), 100 nm (row E) and an extended nanopattern (row F). The cells were either fixed and fluorescently stained on glass substrates (columns 1,2 and 3) or fixed and critical point dried on silicon wafers (columns 4 and 5) on the respective patterns. The red lines and the yellow squares in column 3 highlight the positions of each adhesive patch. FA size is restricted by the underlying pattern geometry if patch sizes are 3 μm or 1 μm, as indicated by the red arrow in A1. On patch sizes $\leq$ 500 nm, adjacent paxillin domains are bridged by an overlying actin fiber, see the red arrow in C1. The borders between neighboring paxillin sites are blurred due to the spatial resolution of optical microscopy. [37]

in figure 8.2 show actin (column 2 and 1, green) and paxillin (column 3 and 1, red). Plated cells showed paxillin rich focal adhesion sites that were constrained to the size and shape of the underlying micro-nanopattern. Paxillin rich domains were exhibited in the case of 3 μm patches (fig. 8.2 row A) to a size of 2.7 ± 0.7 μm and 0.9 ± 0.1 μm in the case of 1 μm patches (fig. 8.2 row B). See also table 8.1 for details. These domains are connected with several (3 μm patches, fig. 8.2 row A) or only one defined actin bundle (1 μm patches, fig. 8.2 row B). In the latter case focal adhesions are restricted to approximately the size of the underlying pattern. However, if the pattern features are smaller than 1 μm, paxillin rich areas are bridged over several domains by one connecting actin bundle. Those paxillin rich domains exhibit sizes of 3.5 ± 0.7 μm (500 nm patches, fig. 8.2 row C) and 2.9 ± 1.1 μm (250nm patches, fig. 8.2 row D). In the case of 100 nm patches (fig. 8.2 row E) the confinement of paxillin enriched domains cannot be resolved by optical microscopy. The domain size in this case 4.7 ± 2.3 μm was about equal to the measured focal adhesion size in the case of an extended homogeneous (non-micro) nanopattern 4.8 ± 2.2 μm. SEM images in fig. 8.2 column 4 and 5 demonstrate this adhesion behavior in higher detail and additionally show the underlying adhesive pattern. Figure 8.3 correlates the size of paxillin rich domains with the size of the underlying pattern.
The measured size differences of paxillin rich domains clearly showed to be dependent on the underlying adhesive pattern. However, the bridging of these domains by actin bundles for patterns smaller than 1 μm could be attributed to local force applied by the actin bundle to the adhesion site. In the case of cells adherent to substrates with 1 μm adhesive sites and bigger the force per patch which is applied by actin bundles and mediated through the adhesive paxillin sites seems to be sufficient to provide stable adhesion. If the area of these adhesive sites is further reduced the force that is needed to mechanically stabilize adhesion is distributed over several smaller subdomains.

The requirement of integrin clustering as a precondition for cell adhesion has been subject of numerous publications like described in section 5.1 and 6.2. However, the exact amount of clustered integrins necessary to induce focal adhesion generation could not be quantified due to insufficient scientific tools. In contrast to earlier interpretations of these results[61] the author states, that with the biofunctionalized nanopatterns used in this work it is now possible to determine this minimum number

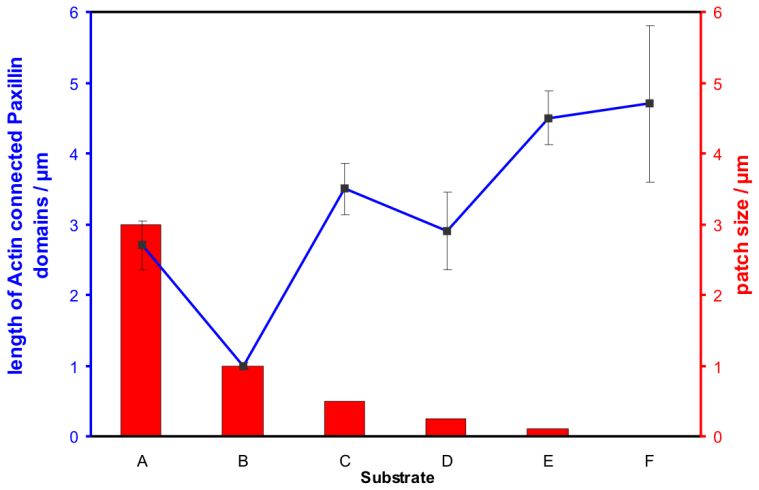

Figure 8.3: Provided surface pattern size (blue) is correlated to the resulting paxilin rich domain size of adherent cells. Letters refer to the respective row of images in figure 8.2. [37]

to 6 integrins that need to cluster in order to induce FA formation. Table 8.1 correlates the micropattern size of the used substrates with the number of gold particles within these adhesive patches. Each gold particle represents one single attachment site for one integrin.

Substrate Patterns	Functionalized gold particles per adhesive patch	Actin-connected paxillin domain length (μm)
3000 nm squares separated by 3000 nm (A)	3007 ± 193	2.7 ± 0.7
1000 nm squares separated by 1000 nm (B)	335 ± 64	0.9 ± 0.1
500 nm squares separated by 500 nm (C)	83 ± 11	3.5 ± 0.7
250 nm squares separated by 250 nm (D)	30 ± 4	2.9 ± 1.1
100 nm squares separated by 100 nm (E)	6 ± 1	4.7 ± 2.3
Extended homogeneous 58 nm gold nanoparticle pattern (F)	-	4.8 ± 2.2

Table 8.1: Pattern characteristics and actin-connected paxillin domain length. Letters in brackets refer to the rows of images in figure 8.2

8.2 Conclusions

Hierarchical nanopatterns were generated by micelle electron beam lithography (MEBL) as described in section 4.1 and used to study the clustering of focal adhesion associated proteins. Taking advantage of the molecular precision and the

defined ligand presentation on the substrate two major results could be obtained.

Firstly, the focal adhesion associated protein paxillin is locally confined to the underlying micro-pattern. Since paxillin resides close to the cell membrane and thus to the substrate surface, its fluorescent staining reveals the basal shape of a focal adhesion. When these confined adhesion sites were $\leq 500\ nm$ bridging of the overlying intracellular actin fibers occurred. This was attributed to distribution of mechanical stress over several adhesive anchor points.

Secondly, the minimum number of integrins that need to cluster in order to induce adhesion has been determined to be 6 ± 1. The used pattern comprised a local spacing of c-RGDfK-thiol funtionalized gold particles of $58nm$ in $100nm$ patches, which equaled a global density of 116 nm spacing on an homogeneous pattern. Therefore the the adhesion process was attribute to integrins clustering.

Generally it can be said, that the use of hierarchical nanopatterns represents a highly valuable tool to study cell adhesion behavior since it provides means of unprecedent precision taking influence on cell behavior.

8.3 Dendritic Cells

8.3.1 Homogeneous Nanopatterns

In order to ensure a cell behavior that is as close to *in vivo* conditions as possible, primary cells have been used for the presented work. Human cells were extracted from buffy coat* from various blood donors and murine cells were obtained from bone marrow of wild type C57/Black 6 mice. Murine DCs have been purified with either a density gradient method (Nycodenz) or additionaly via a magnetic beads kits (MACS) with various antibodies against cell surface receptors. See section 7 for further details. Both methods proved to have high purification efficiencies for DCs although the magnetic beads methods turned out to lead to a heavy unwanted activation of dendritic cells. Thus, cells in all shown experiments have been purified only via the Nycodenz method. All cells have been analyzed using a flow cytometry system to ensure the purity of dendritic cells. Hereby purified cells were fluorescently labeled at cell surface proteins that are specific for DCs like CD11c and scanned for these labeled components during a flow. Due to the accuracy and high cell

*An intermediate layer of a sedimented blood sample mainly consisting of white blood cells

throughput of the method one gains a high statistic certainty that ensures that the used cells really are dendritic cells. Figure 8.4 shows several dot blots of flow cytometry analyses for dendritic cells on day 8 after extraction from bone marrow.

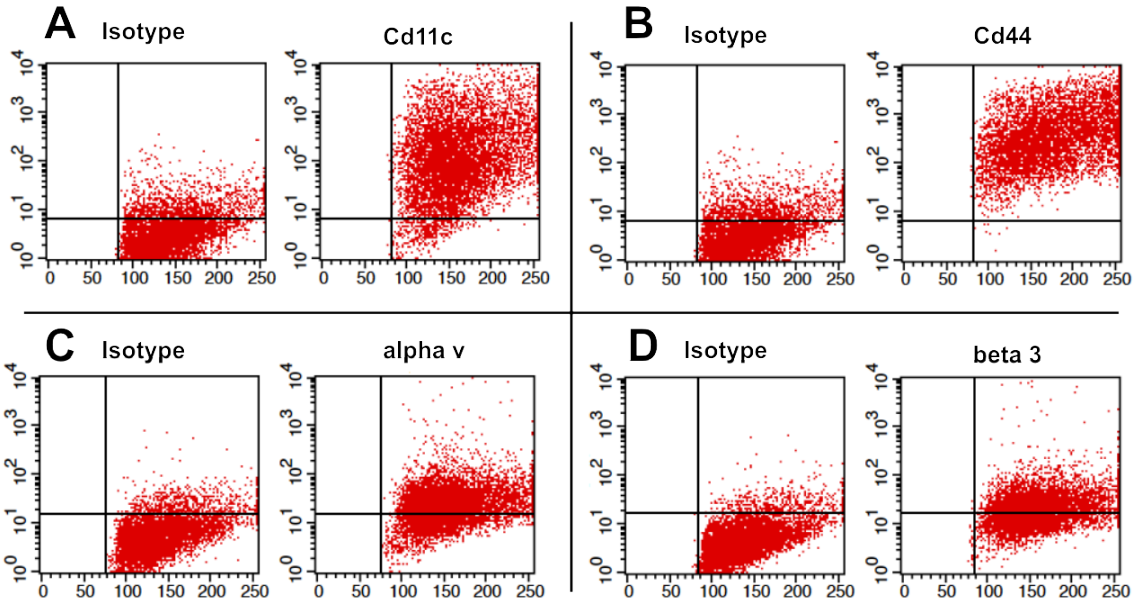

Figure 8.4: Flow cytometry analysis of purified dendritic cells. Graphs show fluorescent intensity (y-axis) against forward scattering (x-axis). Increased fluorescent intensity indicates the presence of the respective protein on the cell surface. Graphs termed 'isotype' are negative controls that indicate unspecific binding of the respective antibody. A and B show upregulation of CD11c and CD44. C and D show upregulation of αv and β3 integrins

Cells were fluorescently stained via monoclonal antibodies against the two integrin monomers αv and β3 and for DC typical surface proteins CD11c and CD44. The blots termed 'isotype' are the negative controls for respective stained protein of interest shown next to it and indicate unspecific labeling. Graphs show fluorescent intensity (y-axis) against forward scattering (x-axis), which is a measure of cell size. Increased fluorescent intensity indicates the presence of the respective protein on the cell surface. Figure 8.4A indicates the expression of CD11c on the cell surface which is termed as a marker for bone marrow derived dendritic cells. CD44 (fig. 8.4B) which has shown to be upregulated in DCs during activation and migration [123] also is clearly present on the cell surface. Additionally, αv and β3 integrins were constantly upregulated during maturation process (Fig 8.4C and D). Murine cells were used at day 8 after extraction from bone marrow since only during this day migration and adhesion was sufficient to obtain results. Human dendritic cells that

were obtained from buffy coat already exhibited the desired state two day earlier. Apart from that no differences in terms of morphology or adhesion and migration behavior between human and murine dendritic cell could be observed. Therefore all images and data derive from murine DCs.

In order to study adhesion behavior c-RGDfK-thiol functionalized nanopatterns have been used as substrate like in section 8.1. Figure 8.5 shows typical SEM images of dendritic cells adherent to an c-RGDfK-thiol functionalized nanostructure of 130 *nm* spacing. Image A shows the typical shape of a dendritic cell and following images show close ups of a specific region of the cell. Image D already reveals the underlying nanopattern and Image E clearly shows that cell-substrate interactions only occur via the gold particles. However, in contrast to experiments with rat embryonic fibroblasts, it turned out not to be of importance on cell behavior how or if at all these particles were functionalized.

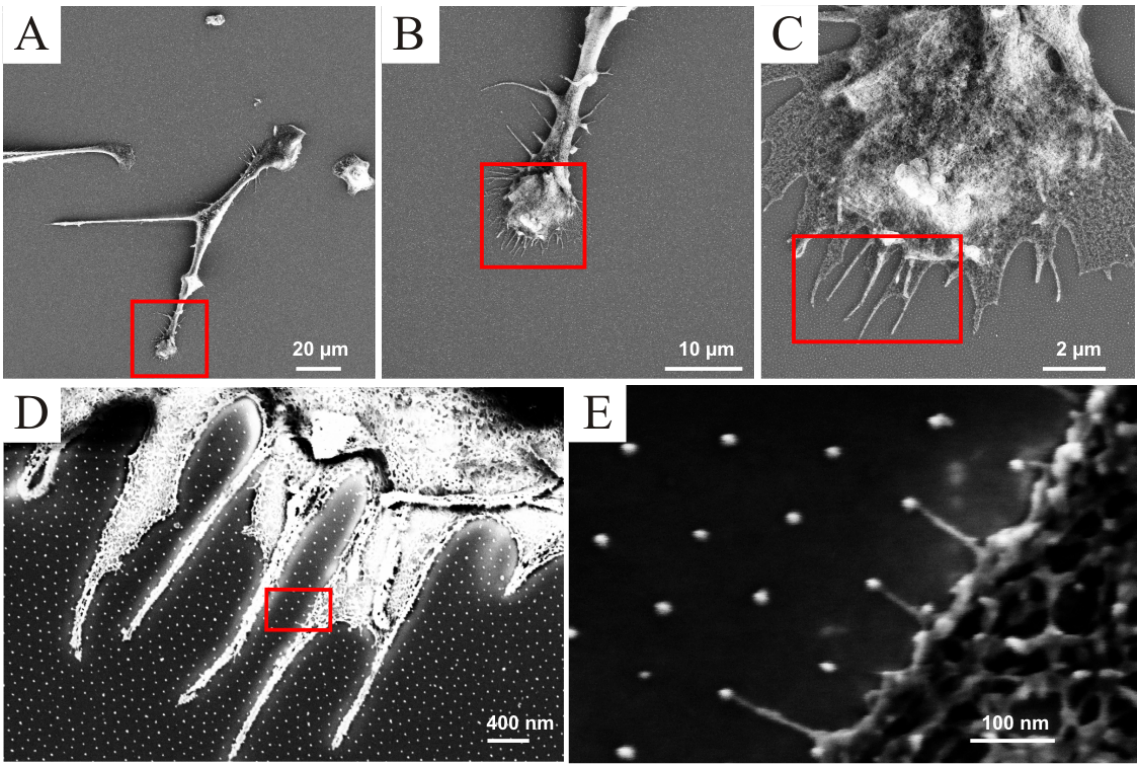

Figure 8.5: SEM images of dendritic cell adherent to nanostructure of 130nm spacing. Red boxes indicate the close up region of the following image. Images A-C were acquired using an SE2-Detector to enhance topographical features, images D and E were acquired using an Inlens detector to enhance material contrast.

Substrates that were coupled with the respective RGE peptide, which served as

a negative control, induced the very same adhesion behavior in dendritic cells. The same applies for nanopatterns that were not coupled at all with peptide. Nonetheless, adhesion only occurred in areas that were patterned with particles. Image A in figure 8.6 indicates this by a clear dipping line. The dipping line is the border of patterned and non-patterned area on the substrate.

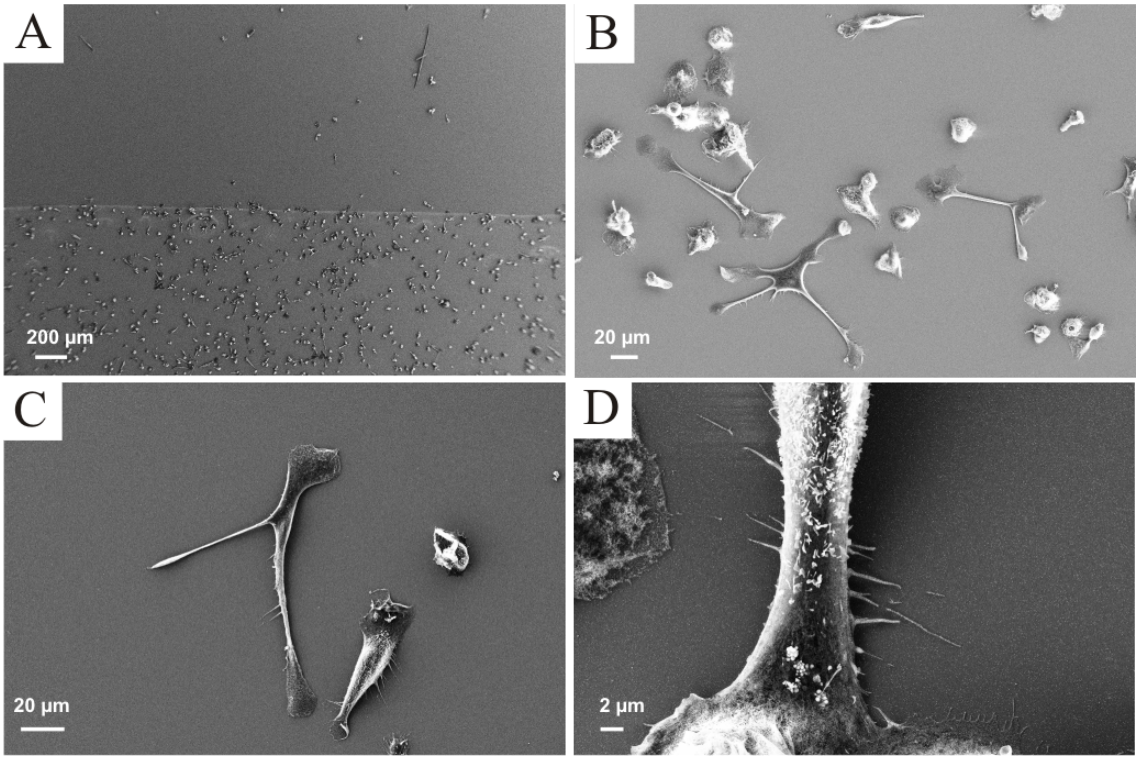

Figure 8.6: Dendritic cells adherent to a biofunctionalized nanostructure of 57 *nm* spacing

Here, the lower part was in contact with the block copolymer solution during the dipping process whereas the upper part was not. Thus, only the lower part bears the nanostructure. Consequently, cells are only found to reside in the lower part of figure 8.6A. This fact served as a proof, that the bound PEG-layer in between the particles still provided sufficient protein repellent qualities. The fact that adhesion occurred independently from the surface bound RGD-peptide indicated that cell-surface interactions might not be integrin mediated. Control experiments on blocking cell membrane integrins by adding RGD-peptide to the cell medium proved this assumption to be true, since cells still were able to adhere to the nanopatterned substrate despite blocked integrins. Other work groups showed comparable adhesion behavior for DCs. Haegel-Kronenberger *et al.* showed that inhibition of several sub-

types of CD44, which is a hyaluronate associated cell adhesion protein, could inhibit adhesion to hyaluronate coated surfaces. But the suppression of adhesion relied on specific combination of of the different CD44 subtypes.[124] A very recent study revealed, that DC adhesion and migration is not necessarily integrin dependent.[125] It proved, that integrin deficient and wild-type DCs did show an indistinguishable adhesion and migration behavior *in vivo* and *in vitro* in artificial three dimensional fibrin matrices. However, integrin mediated cell surface interactions were necessary to provide adhesion to two dimensional substrates. These findings contradict the data presented in this work, since adhesion and migration on nanopatterned substrates within the current setup showed not to be dependent on integrin function. Although the method of integrin deficient cells seems superior to inhibition of integrins by antibodies. Therefore the exact biological background responsible for the adhesion process remains unclear.

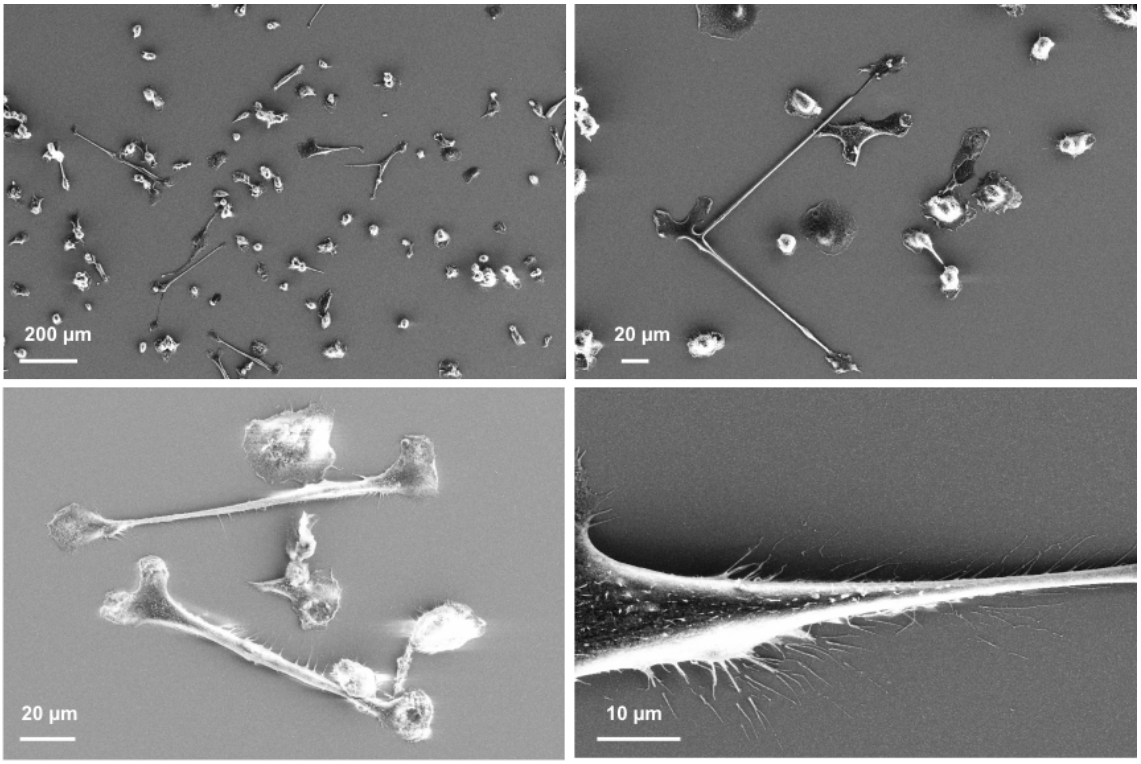

Figure 8.7: Dendritic cells adherent to a biofunctionalized nanostructure of 130 *nm* spacing

Regardless on how the cellular contact to the particles is mediated , the adhesion behavior did depend on the spacing of the underlying pattern; even though to a much

weaker extend than compared to fibroblasts. REF showed an dramatic decrease in cell spreading area when the pattern spacing exceeded $\sim 60\ nm$. Dendritic cells on the other hand were able to spread even on pattern spacings of up to 160 nm with no change in adhesion behavior. Figure 8.6 shows SEM images of critical point dried DCs adherent to a silicon chip with a pattern spacing of 57 nm. Image A shows the already mentioned dipping line and following images illustrate the typical dendritic shape that is also exhibited on non-patterned substrates. Apart from the typical dendrites also very small (200-500 nm) protrusions can be seen that extend sideways from the cell main body as depicted in figure 8.6D. Dendritic Cells also exhibited these morphological features when adherent to a pattern spacing of 130 nm as can be seen in figure 8.7 and 8.5. According to optical microscopy data (not shown) DCs demonstrate an equal behavior in terms of morphology and migration up to a spacing of 160 nm. Spacings $\geq 210\ nm$ were not able to induce adhesion. A defined spacing until which adhesion is still possible like observed for fibroblasts could not be obtained. For dendritic cells a region between 160 nm and 210 nm can be described where obviously a transition takes place that limits the ability of a cells to attach to the substrate. For fibroblasts this phenomenon was attributed to integrins clustering events. Since this adhesion, as discussed above, most probably is not integrin mediated, adhesion effects that depend on spacing can not be traced back to integrin clustering events. Nonetheless, to investigate in this issue hierarchical nanopatterns of gold particles have been produced comparable to the ones used in section 8.1.

8.3.2 Micro-Nanopatterns

In order to subtract potential clustering effects form concentration dependent effects hierarchical nanopatterns of squared patches in different sizes have been produced using resist electron beam lithography described in section 4.2. Since DCs were able to adhere on homogeneous patterns with spacings of 160 nm but not of 210 nm, the spacing for the hierarchical nanopatterns was chosen to be 120 nm. This local spacing at the adhesive patches corresponds to a global density of 240 nm spacing according to equation 2.4 on page 18. Hierarchical nanopatterns with patch sizes of 500 nm, 1 μm 5 μm and 10 μm were generated. Like the substrates shown in figure 4.6 the non-patterned space between the micro-structure had the respective length as the structure itself. That means only a quarter of the area bears the

nano-particles compared to an homogeneous pattern.

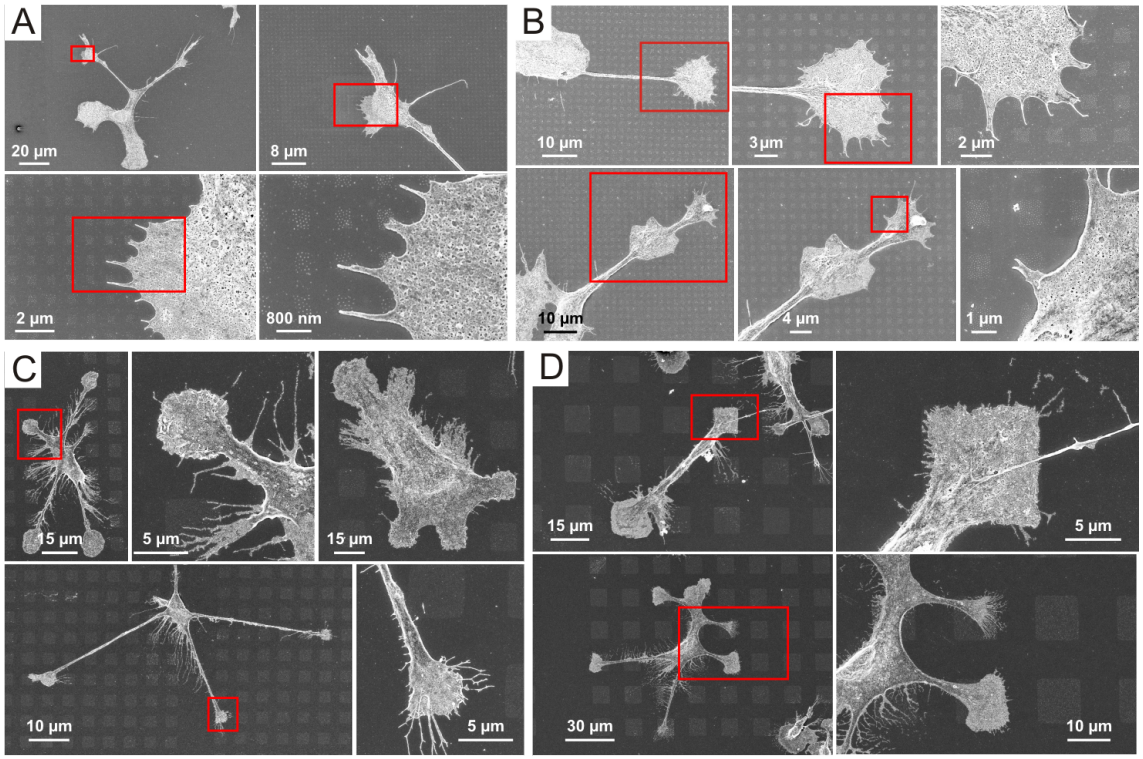

Figure 8.8: SEM images of critical point dried dendritic cells after 3 h seeding on hierarchical nanopattern. Nanopattern spacing of c-RGDfK-thiol functionalized gold particles is 130nm. The nanopattern is present only in squared adhesive patches with edge lengths of 500 nm (A), 1 μm (B), 5 μm (C) and 10 μm (D) that are arranged in a regular array spaced by the distance of the respective edge length. Red boxes indicate close up regions for the image to the right.

Figure 8.8 shows SEM images of critical point dried dendritic cells adherent on an hierarchical c-RGDfK-thiol-functionalized nanopattern with micro-structure features of 500 nm (A), 1 μm (B), 5 μm (C) and 10 μm (D) in size. Surprisingly, cells were able to adhere on the substrate even though the presented global density of this substrate would equal a pattern spacing of 240 nm. Cells showed a clear preference for the adhesive micro patches and thereby exhibited an unusual morphology compared to adherent cells on homogeneous patterns. Each patch comprised 20 (500 nm), 80 (1 μm), 2004 (5 μm) and 8019 (10 μm) particles. Values were calculated according to equation 2.4. SEM images revealed, that distal anchor points of cellular dendrites were able to bridge pattern gaps on adhesive patches of 500 nm and 1 μm (Figure 8.8 A and B) but not on hierarchical structures of 5 μm and 10 μm (C

and D), where anchor points were confined to the design of the underlying pattern. In proximal regions and on dendrites leading to these anchor points cell adhesion obviously was not of great importance since images C and D show, that these parts are able to bridge distances of up to 50 μm of non-adhesive substrate. The ability to bridge considerably larger gaps than fibroblasts studied in section 8.1 could be attributed to the highly migratory competence of dendritic cells.

8.4 Conclusions

Homogeneous and hierarchical nanopatterns that were functionalized with c-RGDfK-thiol were used to study the interplay of osteopontin and dendritic cells. In order to simulate a possible interaction of dendritic cells with the RGD motif of osteopontin cell surface interactions with the described substrates were studied. Although adhesion did depend on particle spacing the biological basis of adhesion mediating interactions remains speculative. The fact that dendritic cells were able to adhere to hierarchically nanopatterned substrates bearing a global particle density of 240 nm, but not on homogeneous patterns with equal density indicate, that the adhesion process is not solely concentration dependent. A possible strategy to pursue this topic might be to study interactions of DCs with the peptide sequence SVVYGLR which also is an integrin binding site of osteopontin. Further on analyzing signaling interactions independently from adhesion mediating processes might be a promising way to elucidate interaction between DCs and osteopontin.

Summarizing, biofunctional nanopatterns proved to be a highly valuable tool to take influence and investigate in cell adhesion. Especially the use of hierarchical nanopatterns turned out to provide substantial knowledge on fundamental cellular processes. The presented micro-nanopatterning techniques now provide a set of different methods that range from single particle deposition to large area patterning. Its utilizations, however, are not necessarily limited to biological interactions and therefore hopefully will yield manifold nanotechnological applications in the future.

List of Figures

Bibliography

[1] L. Royal Society, Nanoscience and Nanotechnology: Opportunities and Uncertainties, *Techn. Ber.*, The Royal Society & The Royal Academy of Engineering, **2004**.

[2] A. A. Seraphin, E. Werwa, K. Kolenbrander, *J. Mater. Res.* **1997**, *12*, 3386–3392.

[3] C. B. Murray, D. J. Norris, M. G. Bawendi, *J. Am. Chem. Soc.* **1993**, *115*(19), 8706–8715.

[4] A. D. Yoffe, *Adv. Phys.* **1993**, *42*(2), 173–262.

[5] G. M. Whitesides, B. Grzybowski, *Science* **2002**, *295*(5564), 2418–2421, DOI 10.1126/science.1070821.

[6] G. M. Whitesides, *Nat. Biotechnol.* **2003**, *21*(10), 1161–1165, DOI 10.1038/nbt872.

[7] S. Zhang, *Nat. Biotechnol.* **2003**, *21*(10), 1171–1178.

[8] D. Philip, J. F. Stoddart, *Angew. Chem. Int. Ed.* **1996**, *35*, 1155–1196.

[9] T. L. Schlick, Z. Ding, E. W. Kovacs, M. B. Francis, *JACS* **2005**, *127*(11), 3718–3723.

[10] G. Felsenfeld, M. Groudine, *Nature* **2003**, *421*(6921), 448–453.

[11] M. Lazzari, C. Rodriguez-Abreu, J. Rivas, M. A. Lopez-Quintela, *J. Nanosci. Nanotechnol.* **2006**, *6*, 892–905(14).

[12] A. Ulman, *Chem. Rev.* **1996**, *96*, 1533–1554.

[13] J. Boneberg, F. Burmeister, C. Schafle, P. Leiderer, D. Reim, A. Fery, S. Herminghaus, *Langmuir* **1997**, *13*(26), 7080–7084.

[14] M. Park, C. Harrison, P. M. Chaikin, R. R. A., D. H. Adamson, *Science* **1997**, *276*, 1401–1404.

[15] L. Rockford, Y. Liu, P. Mansky, T. P. Russell, M. Yoon, S. G. J. Mochrie, *Phys. Rev. Lett.* **1999**, *82*(12), 2602–2605, DOI 10.1103/PhysRevLett.82.2602.

[16] T. L. Morkved, M. Lu, A. M. Urbas, E. E. Ehrichs, H. M. Jaeger, P. Mansky, T. P. Russell, *Science* **1996**, *273*(5277), 931–933.

[17] (Hrsg.: M. Lazzari, G. Liu, S. Lecommandoux), *Block Copolymers in Nanoscience*, (Hrsg.: M. Lazzari, G. Liu, S. Lecommandoux), Wiley-VCH, **2006**.

[18] J. Cheng, C. Ross, H. Smith, E. Thomas, *Adv. Mater.* **2006**, *18*(19), 2505–2521.

[19] T. Yonehara, H. I. Smith, C. V. Thompson, J. E. Palmer, *Appl. Phys. Lett.* **1984**, *45*, 631.

[20] Y. Xia, Y. Yin, Y. Lu, J. McLellan, *Adv. Funct. Mater.* **2003**, *13*(12), 907–918.

[21] R. Segalman, A. Hexemer, R. Hayward, E. Kramer, *Macromolecules* **2003**, *36*(9), 3272–3288.

[22] R. Segalman, A. Hexemer, E. Kramer, *Macromolecules* **2003**, *36*(18), 6831–6839.

[23] R. A. Segalman, A. Hexemer, E. J. Kramer, *Phys. Rev. Lett.* **2003**, *91*(19), 196101–.

[24] Y. Xia, J. A. Rogers, K. E. Paul, G. M. Whitesides, *Chem. Rev.* **1999**, *99*, 1823–1848.

[25] K.-B. Lee, S.-J. Park, C. A. Mirkin, J. C. Smith, M. Mrksich, *Science* **2002**, *295*(5560), 1702–1705.

[26] R. D. Piner, J. Zhu, F. Xu, S. Hong, C. A. Mirkin, *Science* **1999**, *283*, 661–663.

[27] W. Moreau, *Semiconductor Lithography: Principles and materials*, New York:Plenum, **1988**.

[28] D. Brambley, D. Martin, P. Prewett, *Adv. Mater. Opt. Electron.* **1994**, *4*, 55–74.

[29] M. Feldman, J. Sun, *J. Vac. Sci. Technol. B* **1992**, *10*, 3173–3174.

[30] J. P. Silverman, *J. Vac. Sci. Technol. B* **1997**, *15*(6), 2117–2124.

[31] S. Matsui, Y. Kojima, Y. Ochiai, T. Honda, *J. Vac. Sci. Technol., B* **1991**, *9*(5), 2622–2632.

[32] J. Melngailis, *J. Vac. Sci. Technol., B* **1987**, *5*(2), 469–495.

[33] M. A. McCord, *J. Vac. Sci. Technol. B* **1997**, *15*(6), 2125–2129.

[34] C. Vieu, A. Carcenac, Y. Pepin, Y. . Chen, M. Mejias, A. Lebib, L. Manin Ferlazzo, L. Couraud, H. Launois, *Appl. Surf. Sci.* **2000**, *164*, 111–117.

[35] S. Frster, T. Plantenberg, *Angew. Chem. Int. Ed.* **2002**, *41*(5), 688–714.

[36] J. P. Spatz, S. Moessmer, C. Hartmann, M. Moeller, T. Herzog, M. Krieger, P. Boyen, H. G. snd Ziemann, B. Kabius, *Langmuir* **2000**, *16*, 407–415.

[37] M. Arnold, M. Schwieder, J. Bluemmel, E. A. Cavalcanti-Adam, M. Lopez-Garcia, H. Kessler, B. Geiger, J. P. Spatz, *Softmatter* **2009**, in press, DOI 10.1039/b815634d.

[38] C. M. Niemeyer, C. A. Mirkin, *Nanobiotechnology: Concepts, Applications and Perspectives*, Wiley-VCH, **2004**.

[39] C. M. Niemeyer, *Angew. Chem. Int. Ed.* **2001**, *40*(22), 4128–4158.

[40] J. Howard, *Appl. Mech. Rev.* **2002**, *55*, B39.

[41] C. R. Martin, P. Kohli, *Nat. Rev. Drug Discovery* **2003**, *2*(1), 29–37.

[42] X. Yang, A. V. Vologodskii, B. Liu, B. Kemper, N. C. Seeman, *Biopolymers* **1998**, *45*(1), 69–83.

[43] L. Adleman, *Science* **1994**, *266*(5187), 1021–1024.

[44] B. Kasemo, *Curr. Opin. Solid State Mater. Sci.* **1998**, *3*(5), 451–459.

[45] B. Kasemo, *Surf. Sci.* **2002**, *500*(1-3), 656–677.

[46] M. Firestone, M. Shank, S. Sligar, P. Bohn, *J. Am. Chem. Soc.* **1996**, *118*(38), 9033–9041.

[47] S. Vishwanath, D. Bhattacharyya, W. Huang, L. G. Bachas, *J. Membr. Sci.* **1995**, *108*(1-2), 1–13.

[48] T. Wolfram, F. Belz, T. Schoen, J. P. Spatz, *Biointerphases* **2007**, *2*(1), 44–48.

[49] G. Maheshwari, G. Brown, D. Lauffenburger, A. Wells, L. Griffith, *J. Cell Sci.* **2000**, *113*(10), 1677–1686.

[50] M. Arnold, A. Cavalcanti-Adam, R. Glass, W. Blmmel, J. andEck, H. Kessler, J. P. Spatz, *ChemPhysChem* **2004**, *4*, 872–877.

[51] L. Leibler, *Macromolecules* **1980**, *13*, 1602–1617.

[52] F. S. Bates, G. H. Fredrickson, *Annu. Rev. Phys. Chem.* **1990**, *41*, 525557.

[53] G. H. Fredrickson, F. S. Bates, *Annu. Rev. Mater. Res.* **1996**, *26*(1), 501–550.

[54] H.-A. Klok, S. Lecommandoux, *Adv. Mater.* **2001**, *13*(16), 1217–1229.

[55] A. K. Khandpur, S. Foerster, F. S. Bates, I. W. Hamley, A. J. Ryan, W. Bras, K. Almdal, K. Mortensen, *Macromolecules* **1995**, *28*(26), 8796–8806.

[56] K. Edler, *Philos. Trans. R. Soc. London, Ser. A* **2004**, *362*(1825), 2635–2651, DOI 10.1098/rsta.2004.1456.

[57] G. Kaestle, H.-g. Boyen, F. Weigl, G. Lengl, T. Herzog, P. Ziemann, S. Riethmueller, O. Mayer, C. Hartmann, J. P. Spatz, M. Moeller, M. Ozawa, F. Banhart, M. G. Garnier, P. Oelhafen, *Adv. Funct. Mater.* **2003**, *13*, 853–861.

[58] R. Glass, M. Arnold, J. Bluemmel, A. Kueller, M. Moeller, J. P. Spatz, *Adv. Funct. Mater.* **2003**, *13*, 569–575.

[59] J. P. Wilcoxon, B. L. Abrams, *Chem. Soc. Rev.* **2006**, *35*, 1162–1194.

[60] A. Ethirajan, U. Wiedwald, H.-G. Boyen, B. Kern, L. Han, A. Klimmer, F. Weigl, G. Kstle, P. Ziemann, K. Fauth, J. Cai, R. J. Behm, A. Romanyuk, P. Oelhafen, P. Walther, J. Biskupek, U. Kaiser, *Adv. Mater.* **2007**, *19*, 406–410, DOI 10.1002/adma.200601759.

[61] M. Arnold, Dissertation, Universitaet Heidelberg, **2005**.

[62] R. Glass, Dissertation, Universitaet Heidelberg, **2005**.

[63] C. Park, E. L. Yoon, J. amd Thomas, *Polymer* **2003**, *44*, 67256760, DOI 10.1016/j.polymer.2003.08.011.

[64] J. P. Spatz, S. Moessmer, C. Hartmann, M. Moeller, T. Herzog, M. Krieger, H.-G. Boyen, P. Ziemann, B. Kabius, *Langmuir* **2000**, *16*, 407–415.

[65] M. Arnold, V. C. Hirschfeld-Warneken, T. Lohmueller, P. Heil, J. Bluemmel, E. A. Cavalcanti-Adam, M. Lopez-Garcia, P. Walther, H. Kessler, B. Geiger, J. P. Spatz, *Nano Lett.* **2008**, *8*(7), 2063–2069.

[66] T. Lohmller, Dissertation, Universitaet Heidelberg, **2008**.

[67] D. B. Williams, C. B. Carter, *Transmission Electron Microscopy: A Textbook for Materials Science*, Plenum Press New York, London, **1996**.

[68] J. Ackermann, *Manual for the SUPRA (VP) and ULTRA Scanning Electron Microscopes*, Carl Zeiss SMT, Oberkochen, **2005**.

[69] H. Bethe, *Ann. Phys.* **1930**, *397*, 325–400.

[70] J. Goldstein, D. Newbury, D. Joy, C. Lyman, E. Lifshin, L. Sawyer, M. Joseph, *Scanning Electron Microscopy and X-Ray Microanalysis*, Springer - Verlag, **2003**.

[71] H. Niedrig, *Scanning* **1978**, *1*, 17–34.

[72] T. Chang, *J. Vac. Sci. Technol. A* **1975**, *12*, 1271–1275.

[73] R. Glass, M. Moeller, J. P. Spatz, *Nanotechnology* **2003**, *14*, 1153–1160.

[74] R. Glass, M. Arnold, E. A. Cavalcanti-Adam, J. Blummel, C. Haferkemper, C. Dodd, J. P. Spatz, *New J. Phys.* **2004**, *6*, 101.

[75] M. Hatzakis, *J. Electrochem. Soc.* **1969**, *116*, 1033–1037.

[76] W. Eck, A. Kller, M. Grunze, B. Vlkel, A. Glzhuser, *Adv. Mater.* **2005**, *17*(21), 2583–2587.

[77] T. Felgenhauer, C. Yan, W. Geyer, H.-T. Rong, A. Golzhauser, M. Buck, *Appl. Phys. Lett.* **2001**, *79*(20), 3323–3325.

[78] R. M. Steinman, Z. A. Cohn, *J. Exp. Med.* **1973**, *137*(5), 1142–1162.

[79] J. Banchereau, R. M. Steinman, *Nature* **1998**, *392*(6673), 245–252.

[80] J. Banchereau, S. Paczesny, P. Blanco, L. Bennett, V. Pascual, J. Fay, A. K. Palucka, *Ann. N.Y. Acad. Sci.* **2003**, *987*, 180–187.

[81] S. Aiba, *Allergol. Int.* **2007**, *56*, 201–208.

[82] J. Weiss, A. Renkl, C. Maier, M. Kimmig, L. Liaw, T. Ahrens, S. Kon, M. Maeda, H. Hotta, T. Uede, J. Simon, *J. Exp. Med.* **2001**, *194*(9), 1219–1230.

[83] T. Uede, Y. Katagiri, J. Iizuka, M. Murakami, *Microbiol. Immunol.* **1997**, *41*, 641–648.

[84] A. W. O'Regan, G. J. Nau, G. L. Chupp, J. S. Berman, *Immunol. Today* **2000**, *21*(10), 475–478.

[85] D. T. Denhardt, C. M. Giachelli, S. R. Rittling, *Annu. Rev. Pharmacool. Toxicol.* **2001**, *41*(1), 723–749.

[86] L. Liaw, M. Almeida, C. Hart, S. Schwartz, C. Giachelli, *Circ. Res.* **1994**, *74*(2), 214–224.

[87] T.-L. Yue, P. J. Mckenna, E. H. Ohlstein, M. C. Farach-Carson, W. T. Butler, K. Johanson, P. McDevitt, G. Z. Feuerstein, J. M. Stadel, *Exp. Cell. Res.* **1994**, *214*(2), 459–464.

[88] G. Xanthou, T. Alissafi, M. Semitekolou, D. C. M. Simoes, E. Economidou, M. Gaga, B. N. Lambrecht, C. M. Lloyd, V. Panoutsakopoulou, *Nat. Med.* **2007**, *13*(5), 570–578.

[89] B. Geiger, A. Bershadsky, R. Pankov, K. M. Yamada, *Nat. Rev. Mol. Cell Biol.* **2001**, *2*(11), 793–805.

[90] B. Alberts, A. Johnson, J. Lewis, M. Raff, K. Roberts, P. Walter, *Molecular Biology of the Cell*, Garland Science, **2002**.

[91] E. Ruoslahti, *Annu. Rev. Cell Dev. Biol.* **1996**, *12*(1), 697–715.

[92] R. O. Hynes, *Cell* **1987**, *48*(4), 549–554.

[93] R. O. Hynes, *Cell* **2002**, *110*(6), 673–687.

[94] N. Beglova, S. C. Blacklow, J. Takagi, T. A. Springer, *Nat. Struct. Mol. Biol.* **2002**, *9*(4), 282–287.

[95] A. Armulik, I. Nilsson, G. von Heijne, S. Johansson, *J. Biol. Chem.* **1999**, *274*(52), 37030–37034.

[96] R. Li, N. Mitra, H. Gratkowski, G. Vilaire, R. Litvinov, C. Nagasami, J. W. Weisel, J. D. Lear, W. F. DeGrado, J. S. Bennett, *Science* **2003**, *300*(5620), 795–798.

[97] R. Li, C. R. Babu, J. D. Lear, A. J. Wand, J. S. Bennett, W. F. DeGrado, *Proc. Nat. Acad. Sci. U.S.A.* **2001**, *98*(22), 12462–12467.

[98] J.-P. Xiong, T. Stehle, B. Diefenbach, R. Zhang, R. Dunker, D. L. Scott, A. Joachimiak, S. L. Goodman, M. A. Arnaout, *Science* **2001**, *294*(5541), 339–345.

[99] J.-P. Xiong, T. Stehle, R. Zhang, A. Joachimiak, M. Frech, S. L. Goodman, M. A. Arnaout, *Science* **2002**, *296*(5565), 151–155.

[100] R. K. Assoian, *J. Cell Biol.* **1997**, *136*(1), 1–4.

[101] M. A. Schwartz, R. K. Assoian, *J. Cell Sci.* **2001**, *114*(14), 2553–2560.

[102] R. Fassler, M. Meyer, *Genes Dev.* **1995**, *9*(15), 1896–1908.

[103] J. Yang, H. Rayburn, R. Hynes, *Development* **1995**, *121*(2), 549–560.

[104] D. Taverna, M.-H. Disatnik, H. Rayburn, R. T. Bronson, J. Yang, T. A. Rando, R. O. Hynes, *J. Cell Biol.* **1998**, *143*(3), 849–859.

[105] J. Zhu, K. Motejlek, D. Wang, K. Zang, A. Schmidt, L. F. Reichardt, *Development* **2002**, *129*(12), 2891–2903.

[106] J. H. McCarty, R. A. Monahan-Earley, L. F. Brown, M. Keller, H. Gerhardt, K. Rubin, M. Shani, H. F. Dvorak, H. Wolburg, B. L. Bader, A. M. Dvorak, R. O. Hynes, *Mol. Cell. Biol.* **2002**, *22*(21), 7667–7677.

[107] B. L. Bader, H. Rayburn, D. Crowley, R. O. Hynes, *Cell* **1998**, *95*(4), 507–519.

[108] M. Abercrombie, G. A. Dunn, *Exp. Cell. Res.* **1975**, *92*(1), 57–62.

[109] E. Zamir, B. Geiger, *J. Cell Sci.* **2001**, *114*(20), 3583–3590.

[110] D. Riveline, E. Zamir, N. Q. Balaban, U. S. Schwarz, T. Ishizaki, S. Narumiya, Z. Kam, B. Geiger, A. D. Bershadsky, *J. Cell Biol.* **2001**, *153*(6), 1175–1186.

[111] S. Miyamoto, H. Teramoto, O. Coso, J. Gutkind, P. Burbelo, S. Akiyama, K. Yamada, *J. Cell Biol.* **1995**, *131*(3), 791–805.

[112] J. C. Adams, *Cell. Mol. Life Sci.* **2001**, *58*, 371 – 392.

[113] R. Haubner, W. Schmitt, G. Holzemann, S. Goodman, A. Jonczyk, H. Kessler, *J. Am. Chem. Soc.* **1996**, *118*(34), 7881–7891.

[114] M. Kantlehner, P. Schaffner, D. Finsinger, J. Meyer, A. Jonczyk, B. Diefenbach, B. Nies, G. Hlzemann, S. L. Goodman, H. Kessler, *ChemBioChem* **2000**, *1*(2), 107–114.

[115] G. Kenausis, J. Voros, D. Elbert, N. Huang, R. Hofer, L. Ruiz-Taylor, M. Textor, J. Hubbell, N. Spencer, *J. Phys. Chem. B* **2000**, *104*(14), 3298–3309.

[116] B. Zdyrko, V. Klep, I. Luzinov, *Langmuir* **2003**, *19*(24), 10179–10187.

[117] B. Zdyrko, S. Varshney, I. Luzinov, *Langmuir* **2004**, *20*(16), 6727–6735.

[118] J. H. Lee, H. B. Lee, J. D. Andrade, *Prog. Polym. Sci.* **1995**, *20*(6), 1043–1079.

[119] J. Bluemmel, N. Perschmann, D. Aydin, J. Drinjakovic, T. Surrey, M. Lopez-Garcia, H. Kessler, J. P. Spatz, *Biomaterials* **2007**, *28*(32), 4739–4747.

[120] K. Inaba, M. Inaba, N. Romani, H. Aya, M. Deguchi, S. Ikehara, S. Muramatsu, R. Steinman, *J. Exp. Med.* **1992**, *176*(6), 1693–1702.

[121] C. Turner, *J. Cell Sci.* **2000**, *113*(23), 4139–4140.

[122] E. A. Cavalcanti-Adam, T. Volberg, A. Micoulet, H. Kessler, B. Geiger, J. P. Spatz, *Biophys. J .* **2007**, *92*(8), 2964–2974, DOI 10.1529/biophysj.106.089730.

[123] J. M. Weiss, J. Sleeman, A. C. Renkl, H. Dittmar, C. C. Termeer, S. Taxis, N. Howells, M. Hofmann, G. Kohler, E. Schopf, H. Ponta, P. Herrlich, J. C. Simon, *J. Cell Biol.* **1997**, *137*(5), 1137–1147.

[124] H. Haegel-Kronenberger, H. de la Salle, A. Bohbot, F. Oberling, J.-P. Cazenave, D. Hanau, *J. Immunol.* **1998**, *161*(8), 3902–3911.

[125] T. Laemmermann, B. L. Bader, S. J. Monkley, T. Worbs, R. Wedlich-Soldner, K. Hirsch, M. Keller, R. Forster, D. R. Critchley, R. Fassler, M. Sixt, *Nature* **2008**, *453*(7191), 51–55.

Acronyms

APC antigen presenting cell

BCML block copolymer micellar lithograpghy

BSA bovine serum albumin

BSE backscattered electrons

CL cathodoluminescense

DMEM dulbecco's modified eagle medium

DNA deoxyribonucleic acid

DC dendritic cell

ECM extracellular matrix

FA focal adhesion

FITC fluorescein isothiocyanate

GCM-CSF granulocyte macrophage colony-stimulating factor

GAG glycosaminoglycans

ICAM-1 inter-cellular adhesion molecule 1

LPS lipopolysaccharide

MACS Magnetic Cell Sorting of Human Leukocytes

MEBL micelle electron beam lithography

min minutes

MHC major histocompatibility complex

OPN osteopontin

PBS phosphate buffered saline

PE primary electrons

PEG poly(ethylene glycol)

PS polystyrene

PVP poly-2-vinyl-pyridine

REF rat embryonic fribroblast

RGD arginine-glycine-aspartate

RPM revolutions per minute

RT room temperature

SC specimen currents

SE secondary electrons

SEM scanning electron microscopy

TE transmitted electrons

TRITC tetramethyl rhodamine iso-thiocyanate

TSA templated self assembly

QCM quartz crystal micro balance

YFP yellow fluorescent protein

Danksagung

Zuallererst möchte ich mich bei Herrn Prof. Dr. Joachim P. Spatz bedanken. Er hat mir die Möglichkeit gegeben in diesem faszinierenden interdisziplinren Umfeld von Materialwissenschaft, Nanotechnologie und Biologie zu arbeiten. Ich habe die abwechslungsreiche Tätigkeit sehr genossen und ihre Faszination hat mich bis zum Ende meiner Doktorarbeit begleitet. Vielen Dank auch für die zahlreichen Möglichkeiten meine Arbeit außerhalb der Gruppe und im Ausland zu präsentieren und für den immer ruhigen und freundlichen Umgang. Herzlichen Dank auch an den Rest der Prüfungskommission, Herrn PD Dr. Reiner Dahint, Herrn Prof. Dr. Johannes Weiss und Herrn Prof. Dr. Peter Comba für die Flexibilitt bezüglich. des Prüfungstermins und deren spontane Zusagen sich als Prüfer beziehungsweise Gutachter zur Verfügung zu stellen.

Bei Dr. Marco Arnold möchte ich mich herzlich bedanken, der mich experimentell in die Mikro-Nanowelt eingeführt hat. Nochmals Dank an Herrn Prof. Dr. Weiss. Das Projekt der dendritischen Zellen wäre ohne ihn nicht möglich gewesen. In diesem Zusammenhang auch vielen Dank an Franziska Buback für die angenehme Zusammenarbeit, die Bereitstellung der dendritischen Zellen, die ständigen Fahrten nach Stuttgart und vieles mehr. Ich möchte mich bei Daniel Aydin und Dr. Theobald Lohmüller für die effektive Zusammenarbeit bei der Resist- und der Flood Gun Lithographie bedanken. Speziellen Dank auch an Ferdinand Belz und Tobias Schön für die Synthetisierung des m-PEG-urea 2000.

Während meines Aufenthalts am Max-Planck-Institut hatte ich die Gelegenheit einige “Office Homies” kennenzulernen bei denen ich mich für die immer freundliche und witzige Arbeitsatmosphäre bedanken möchte. Diese waren: Alex de Beer, Sarah Biela, Ferdinand Belz, Timo Burek, Lisa Maus, Petra Salame, Stefan Kudera, Ian Dunlop, Peter Kaiser, Christine Mollenhauer und Henriette Ries. Ich hoffe ich habe niemanden vergessen. Viele Arbeiten werden einem erleichtert wenn man auf wichtige Leute zurückgreifen kann. Ich möchte mich hier im Speziellen bei Margit

Kapp, Maria Sycha and Janis Grigoridis bedanken, die mir zahllose Goldpunktsubstrate zur Verfügung gestellt haben, vorallem wenn die Zeit mal wieder knapp war. Vielen Dank an Dr. Theobald Lohmüller, Dr. Ralf Kemkemer, Daniel Aydin, Ilia Louban, Dr. Babak Hosseini und Peter Kaiser für das Korrekturlesen meiner Arbeit.

Nicht zuletzt, liebe Spatz-Gruppe, vielen Dank Euch allen, für die schöne Zeit die ich hatte und die unvergesslichen Aufenthalte in der Toskana, Antholz, Weingarten und natürlich am Tegernsee. Danke auch an die Istanbul Crew für die coole Zeit.

Last - not least, einen großen Dank an meine Eltern, die mich während des gesamten Studiums und der Zeit meiner Doktorarbeit durchgehend untertützt haben, egal welche Entscheidung ich auch getroffen habe.

Ich erkläre hiermit, dass ich die vorgelegte Dissertation selbst verfasst und mich keiner anderen als der von mir ausdrücklich bezeichneten Quellen und Hilfen bedient habe.

Stuttgart, 9. Dezember 2008 .....

Marco Schwieder